DARK CURRENT MECHANISMS AND PASSIVATION OF InAsSb INFRARED PHOTODIODES ON ALTENATIVE SUBSTRATES

A THESIS SUBMITTED TO
THE GRADUATE SCHOOL OF NATURAL AND APPLIED SCIENCES
OF
MIDDLE EAST TECHNICAL UNIVERSITY

BY

ÖZLEM ERSAGUN

IN PARTIAL FULFILLMENT OF THE REQUIREMENTS
FOR
THE DEGREE OF MASTER OF SCIENCE
IN
ELECTRICAL AND ELECTRONICS ENGINEERING

DECEMBER 2005

Approval of Graduate School of Natural and Applied Sciences.

____

Prof. Dr. Canan ÖZGEN

Director

I certify that this thesis satisfies all the requirements as a thesis for the degree of Master of Science.

____

Prof. Dr. İsmet ERKMEN

Head of Department

This is to certify that we have read this thesis and that in our opinion it is fully adequate, in scope and quality, as a thesis for the degree of Master of Science.

____

Prof. Dr. Cengiz BEŞİKCİ

Supervisor

Examining Committee Members:

Prof. Dr. Nevzat Güneri GENCER	(METU, EE)	____________
Prof. Dr. Cengiz BEŞİKCİ	(METU, EE)	____________
Prof. Dr. Mehmet PARLAK	(METU, PHYS)	____________
Asst. Prof. Dr. Yeşim SERİNAĞAOĞLU	(METU, EE)	____________
Asst. Prof. Dr. Haluk KÜLAH	(METU, EE)	____________

I hereby declare that all information in this document has been obtained and presented in accordance with academic rules and ethical conduct. I also declare that, as required by these rules and conduct, I have fully cited and referenced all material and results that are not original to this work.

Name, Last Name :

Signature :

ABSTRACT

DARK CURRENT MECHANISMS AND PASSIVATION OF InAsSb INFRARED PHOTODIODES ON ALTERNATIVE SUBSTRATES

ERSAGUN, Özlem

M.Sc., Department of Electrical and Electronics Engineering

Supervisor: Prof. Dr. Cengiz BEŞİKCİ

December 2005, 64 pages

This thesis reports a detailed characterization of indium arsenide antimonide ($InAs_{1-x}Sb_x$) photodetectors grown on gallium arsenide (GaAs) substrate by molecular beam epitaxy. A combination of polyimide and sulphur and a single layer of polyimide were used as passivation films in this study. Two different epilayer structures were used for assessing the detector performance and comparing the above passivation layers. For the first structure, the optical measurements revealed that Sb mole fraction was 0.13 and the cut-off wavelength was around 4.1 μm at 80 K. The Sb mole fraction of the second structure was 0.2, and the 77 K cut-off wavelength was 4.8 μm. Detailed electrical and optical characterizations were performed on 33x33 μm^2 test diodes. The photodiodes yielded peak detectivities of $\sim 3.65 \times 10^{10}$ and $\sim 1.22 \times 10^{10}$ $cmHz^{1/2}/W$ at 80 K for the first and second structures, respectively. Considerable $1/f$ noise current related with trap-assisted tunneling

mechanism was observed in both structures at 80 K.

Dark current modeling study showed that the dark current was dominated by the shunt and trap-assisted tunneling mechanisms throughout the entire reverse bias voltages for both detectors. The dark current analysis of variable area detectors fabricated with both epilayer structures revealed that the reverse bias current was mainly generated by the surface leakage in small sized (33x33 μm^2) detectors for both passivation layers. However, the surface current contribution was observed to be lower for the double layer (polyimide and sulphur) passivated detectors suggesting that it is a better passivation technique.

Keywords: photodetector, InAsSb, passivation.

ÖZ

ALTERNATİF TABANLAR ÜZERİNDEKİ InAsSb KIZILÖTESİ FOTODİYOTLARIN KARANLIK AKIM MEKANİZMALARI VE PASİVASYONU

ERSAGUN, Özlem
Yüksek Lisans, Elektrik Elektronik Mühendisliği Bölümü
Tez Yöneticisi: Prof. Dr. Cengiz BEŞİKCİ

Aralık 2005, 64 sayfa

Bu tez galyum arsenik (GaAs) taban üzerinde moleküler ışın epitaksisi tekniğiyle büyütülen indiyum arsenik antimon ($InAs_{1-x}Sb_x$) fotodedektörler üzerindeki detaylı karakterizasyonu rapor etmektedir. Bu tezde sülfür ve polyimide kombinasyonu ve tek katman polyimide pasivasyon filmleri olarak kullanılmıştır. Dedektör performansının değerlendirilmesi ve yukarıdaki pasivasyon tekniklerinin karşılaştırılması için iki farklı epitaksiyel katman yapısı kullanılmıştır. Optik ölçüm sonuçları ilk yapı için Sb mol oranının 0.13 ve kesim dalga boyunun 80 K sıcaklıkta 4.1 μm civarında olduğunu göstermiştir. İkinci yapıda Sb mol oranı 0.2 ve 77 K sıcaklıktaki kesim dalga boyu 4.8 μm olarak gözlenmiştir. Detaylı elektriksel ve optik karakterizasyonlar 33x33 μm^2 alanlı test diyotları üzerinde yapılmıştır. Birinci ve ikinci yapılar için fotodiyotların 80 K sıcaklıkta dedektivite

değerleri sırasıyla ~3.65×10^{10} ve ~1.22×10^{10} cmHz$^{1/2}$/W olarak ölçülmüştür. Her iki yapıda da 80 K sıcaklıkta tuzak yardımlı tünelleme mekanizmasından kaynaklanan dikkate değer ölçüde $1/f$ gürültü akımı gözlenmiştir.

Karanlık akım modellemesi çalışması, her iki yapı için de ters eğimleme gerilimleri altında karanlık akımın paralel ve tuzak yardımlı tünelleme mekanizmalarıyla belirlendiğini göstermiştir. Her iki epikatman yapı üzerinde fabrike edilen değişik alanlı dedektörlerin karanlık akım analizleri, küçük alanlı (33x33 μm^2) dedektörlerde ters eğimleme akımının her iki pasivasyon katmanı için de çoğunlukla yüzey kaçakları tarafından oluşturulduğunu ortaya çıkarmıştır. Bununla birlikte, çift katmanla (polyimide ve sülfür) pasive edilmiş dedektörler için yüzey akımının katkısının daha az olduğu gözlenmiş ve bu pasivasyon tekniğinin daha uygun olduğu izlenimine varılmıştır.

Anahtar Kelimeler: fotodedektör, InAsSb, pasivasyon.

To my grandfather

ACKNOWLEDGMENTS

I would like to thank my thesis supervisor Prof. Dr. Cengiz Beşikçi for his guidance and supports throughout my graduate study. I would also like to thank him for giving me a chance to work with his research group.

I have to thank very much to Ümid Tümkaya for his support in the fabrication process. I would also like to thank Burak Aşıcı for his collaboration in the electrical testing, to Oray Orkun Cellek for his help in the optical characterization and to Selçuk Özer for his helpful discussions throughout my study. I want to express my gratitude to Sema Memiş for her support and motivation. I would also like to thank to Umut Bostancı, Hasan Koçer, Melih Kaldırım, Süleyman Eker and other members of our research group.

Finally, I must express my endless gratitude to my family for their invaluable support and encouraging.

TABLE OF CONTENTS

PLAGIARISM……………………………………..iii

ABSTRACT..iv

ÖZ vi

ACKNOWLEDGMENTS ix

TABLE OF CONTENTS………………………………………………………...x

CHAPTER

1. INTRODUCTION...1

1.1 Basics of Infrared Radiation 2

1.2 Infrared Detector Types 5

1.3 Detector Performance Parameters 9

2. InSb, $InAs_{1-x}Sb_x$ and $Hg_{1-x}Cd_xTe$ DETECTOR TECHNOLOGIES....................11

2.1 InSb Detectors...11

2.2 InAsSb Detectors 13

2.3 HgCdTe Detectors 17

2.4 Passivation Techniques used for InSb Based Materials 18

3. TEST DETECTOR FABRICATION AND ELECTRICAL CHARACTERIZATION 23

3.1 Epilayer Structures Used For Test Detector Fabrication 23

3.2 Test Detector Fabrication....24
3.3 Characterization of the Test Detectors....27
3.3.1 Characterization of $InAs_{1-x}Sb_x$ Detector....29
3.3.1.1 Electrical Characteristics....29
3.3.1.2 Optical Characteristics....30
3.3.1.3 Noise Current Analysis....32
3.3.2 Characterization of $InAs_{0.8}Sb_{0.2}$ Detector....34
3.3.2.1 Electrical Characteristics....34
3.3.2.2 Optical Characteristics....36
3.3.2.3 Noise Current Analysis....36
4. DARK CURRENT MODELLING....39
4.1 Dark Current Analysis....39
4.1.1 Diffusion Current....39
4.1.2 Generation-Recombination Current....41
4.1.3 Tunneling Current....43
4.1.4 Ohmic Leakage Current....45
4.1.5 Dark Current Modelling of $InAs_{1-x}Sb_x$/GaAs Detector....45
4.1.6 Dark Current Modeling of $InAs_{0.8}Sb_{0.2}$/GaAs Detector....52
5. CONCLUSIONS....60
REFERENCES....62

CHAPTER I

INTRODUCTION

Infrared (IR) radiation is an electromagnetic wave, which has wavelengths shorter than microwave radiation but longer than the visible light. Infrared radiation has wavelengths between 700 nm and 1 mm.

Infrared detectors sensing in the atmospheric windows of 3-5 μm (MWIR) and 8-12 μm (LWIR) have widely been used for numerous thermal imaging applications. $InAs_{1-x}Sb_x$ is an important alloy for sensing in these windows. Growth of infrared materials on GaAs or Si substrates is indispensable for low cost fabrication of large format infrared sensor arrays (so called focal plane array, FPA). This thesis reports a study on the investigation of the characteristics of $InAs_{1-x}Sb_x$ infrared sensors grown on alternative (GaAs) substrates with molecular beam epitaxy. The study also investigates the performance of different passivation techniques on these sensors grown with lattice mismatched epitaxy.

The scope of this thesis work is as follows:

- $InAs_{1-x}Sb_x$ test detectors were fabricated on GaAs substrates. Two different passivation layers were investigated for each structure.

- Detailed characterization was performed to assess the performance of the fabricated test detectors.

- Detailed dark current modeling was done in order to identify the dominant dark current mechanisms under different bias voltages at 77 K. For the dark current analysis, measured data was fitted to the sum of the expressions for various dark current mechanisms. The fitting results for different passivation layers were compared and results were interpreted.

The organization of this thesis work is as follow:

The following sections present the fundamentals of IR radiation, infrared detector types and important detector performance parameters.

Chapter II presents the InSb, InAsSb, and HgCdTe detector technologies. This chapter also includes a literature survey on the passivation studies made by other research groups on InSb based detectors.

Chapter III presents the fabrication of test detectors, electrical and optical characterization, and noise current analysis.

Chapter IV presents the dark current modeling and analysis of I-V characteristics of variable area test detectors. The interpretation of the results is also given in this chapter. Finally, Chapter V presents the conclusions of this study.

1.1 Basics of Infrared Radiation

Every object at a temperature above absolute zero emits infrared radiation, and this radiation is absorbed by different compounds found in the atmosphere. There are four main windows: 1 –3 μm range Short Wave Infrared (SWIR), the 3-5 μm range

Mid Wave Infrared (MWIR), the 8-12 μm range Long Wave Infrared (LWIR) and the 12-25 μm range Very Long Wave Infrared (VLWIR).

Radiation is either absorbed or scattered when it propagates in the atmosphere which causes attenuation of the radiation. In the MWIR and LWIR atmospheric windows, atmospheric transmission is maximum. Therefore infrared imaging is usually performed in these windows. The MWIR region is more suitable for hotter objects. The LWIR region corresponds to the emission from objects at the room temperature. Figure 1.1 gives a plot of the atmospheric transmission as a function of wavelength.

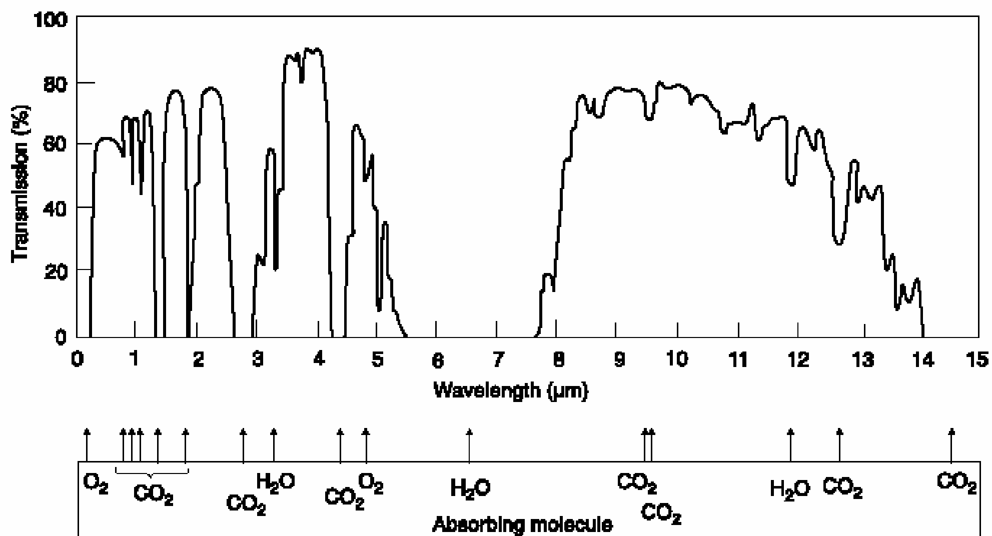

Figure 1.1: Atmospheric transmission through 6000ft sea level path [1].

Power emitted by the bodies at different temperatures can be calculated by using Planck's law (1900). Spectral radiant emittance of a blackbody is given as [2]

$$M_q(\lambda,T) = \frac{2\pi c}{\lambda^4\left(e^{hc/\lambda kT} - 1\right)} \tag{1.1}$$

where λ (μ) is wavelength, T (K) is temperature, h (Wsec^2) is Planck's constant, c is the velocity of light, and k is the Boltzmann's constant (WsecK^{-1}). The radiant

power versus wavelength curve derived from Planck's equation for different temperatures is given in Figure 1.2.

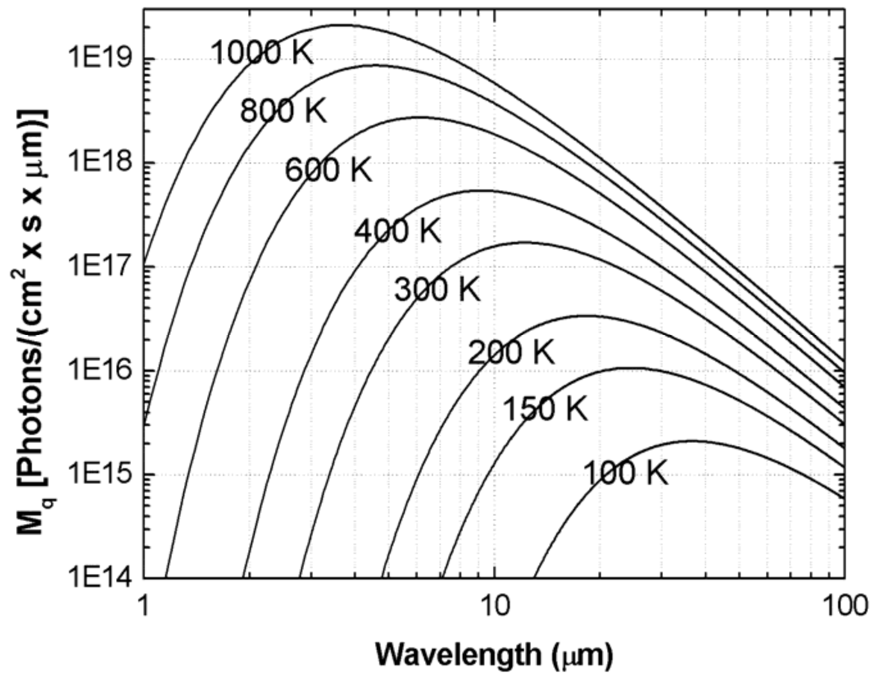

Figure 1.2: Radiant power versus wavelength curve [3].

It can be seen that at low temperatures the emitted power is low. As the temperature increases, the amount of energy emitted at any wavelength increases while the peak wavelength shifts to shorter wavelengths. Peak emission wavelength can be obtained from Wien's displacement law,

$$\lambda_{\max} = \frac{2898}{T} \tag{1.2}$$

where λ_{max} (μm) is the wavelength, and T (K) is temperature. It is inferred that hot bodies radiate at shorter wavelengths.

1.2 Infrared Detector Types

Infrared detectors can be classified into two main groups: Thermal detectors and photon (quantum) detectors.

Thermal detectors convert incident radiation into heat, thereby changing the temperature of the detector element. Change in temperature alters some temperature sensitive quantities such as resistance, current or voltage. These resultant change is used to generate an electrical signal.

The response of the thermal detectors is independent of wavelength, because they rely only on the total amount of heat transferred to the detector by the absorption of the light. They can operate at room temperature, which makes them less costly and easy to use for civil applications. Since the operation of thermal detectors depends on the temperature change, they have slower response times and lower sensitivies than photon detectors, which limit their use in some military applications.

There are four widely used thermal detectors: Bolometers, thermocouples or thermopiles, pyroelectric detectors and golay cells. Bolometer is basically a resistive element. In bolometers, changes in resistance occur, if the detector absorbs incident radiation. To improve the sensitivity of the bolometer, the resistive material with a small heat capacity and a large temperature coefficient should be used, so that significant changes in conductance occur when the detector absorbs IR radiation.

Thermocouples are formed by joining two dissimilar conductors that create voltages at their junctions. Thermopiles consist of a number of thermocouples connected to increase the responsivity. IR radiation absorbed by these devices can be detected by monitoring the voltage generated by the thermocouples or thermopiles. For more sensitive detection, these devices must be insulated from their surroundings.

In pyroelectric detectors, the polarization or surface charge changes with temperature. Absorption of the IR radiation causes fluctuation in the polarization and thus an alternating current that can be monitored with an external circuit. The Golay cell uses the pressure or volume changes in a gas to monitor the absorption of radiation.

In photon (quantum) detectors, when a photon with energy greater than the band gap is absorbed, free charge carriers, which is an electron in the conduction band and a hole in the valance band, are generated. The equation below gives the relationship between the energy of the photon and the wavelength of the radiation.

$$E = \frac{hc}{\lambda} \tag{1.3}$$

where h is Planck's constant, c is the speed of light and λ is the wavelength.

The temperature of the photon detector must be low enough in order to decrease the number of the carriers thermally excited across the bandgap. To keep the detector temperature at low levels, dewar or cooling system is required which increases the cost of the photon detectors.

Photons of larger wavelengths have less energy. If incident photon has energy lower than the bandgap of the semiconductor, it will not be absorbed and pass through the material. Cutoff wavelength shows the maximum wavelength beyond which the detector is transparent. Most of the photon absorption occurs over a distance 1/α [4], where α is the absorption coefficient of the semiconductor material. This distance is called the penetration depth. Not all of the absorbed photons may create free carriers that can be collected as a photocurrent. If the absorption coefficient is too large, the absorption occurs near the surface or outside the depletion region, where there is no electric field. Therefore some of these carriers recombine and disappear without reaching the depletion layer.

The number of the electron-hole pairs crossing the junction per incident photon is called the quantum efficiency (η). The absorption of every photon does not produce a free carrier reaching the junction, so η is usually less than unity. The quantum efficiency can be increased by reducing the reflection at the semiconductor surface and increasing the absorption within the junction.

The detection mechanism in photon detectors is based on the generation of these free charge carriers. Photon detectors can be classified as intrinsic, extrinsic, photoemissive and quantum well infrared photodetectors (QWIP's) [5]. Both photoconductive and photovoltaic types exist for intrinsic and extrinsic photon detectors.

When infrared radiation is absorbed by the photoconductive detectors, the photoexcited carriers change the conductivity of the material, and an external circuit is used to measure this change in the conductivity. Either intrinsic or extrinsic semiconductors can be used for the fabrication of photoconductors.

Figure 1.3 shows the simplified structure of the typical photovoltaic sensor (p-n junction photodiode).

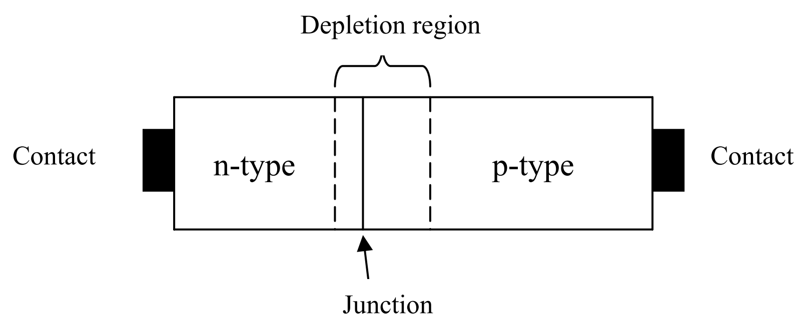

Figure 1.3: Simplified structure of a p-n photovoltaic diode.

In this structure, one side of the semiconductor is doped to produce an excess of holes and the other side is doped to produce an excess of electrons. At the p-n junction, electrons and holes diffuse from one side to the other side because of the concentration gradient. Holes diffusing into the n side recombine with the electrons,

and similarly electrons diffusing into the p side recombine with the holes. Therefore, depletion region is created. There is an internal electric field in the depletion region. This field sweeps the carriers in the opposite direction of the diffusion process. When the IR radiation is absorbed, free charge carriers are generated. These carriers, produced in the depletion layer, are separated by the electric field and sweep across the junction. Charge carriers in the neutral region diffuse to the depletion region and drift across the junction. This resulting drift current generates a photocurrent. This photocurrent is given as [5]

$$I_{ph} = \eta q A \Phi \tag{1.4}$$

where η is the quantum efficiency which is the number of electron-hole pairs crossing the junction per incident photon, A is the area of the detector, and Φ is the incident radiation photon flux.

The I-V characteristic of the photovoltaic diode is shown in Figure 1.4.

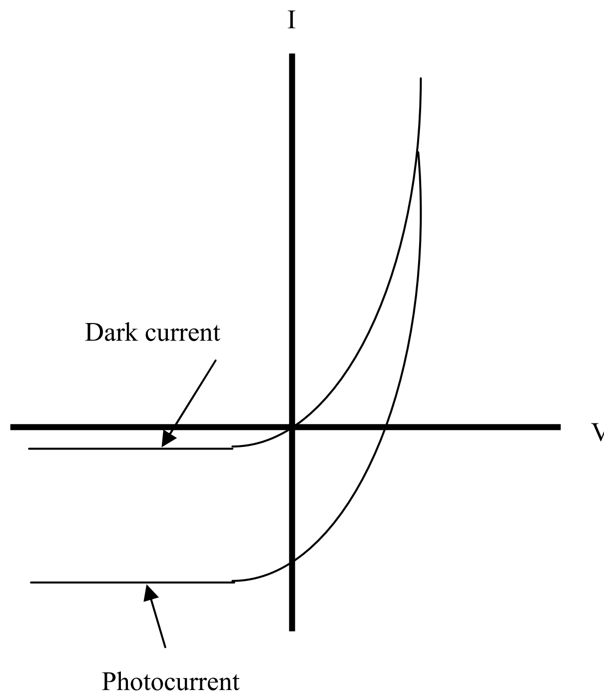

Figure 1.4: I-V curve of a photodiode.

Photovoltaic detectors must be cooled to cryogenic temperatures to eliminate thermally generated carriers. Cooling is especially important for the detectors fabricated from small bandgap semiconductors. To obtain high quantum efficiency in photovoltaic detectors, incident radiation should be absorbed within a diffusion length of the junction; consequently the junction depth should be small compared to diffusion length of the carriers, and materials with high absorption coefficient should be used. Photovoltaic detectors do not require bias supply, hence they have low power dissipation, and they can be directly coupled into the read out circuit without requiring an interfacing amplifier.

1.3 Detector Performance Parameters

In order to characterize an IR detector and compare the performance of the different detectors, it is necessary to use the detector parameters. The most important ones are briefly discussed below.

Responsivity: Responsivitiy (R) is defined as the ratio between the output signal and the incidence power. The unit of the responsivity can be Volts/ Watt or Amp/ Watt. R is given by

$$R = \frac{Output\ Signal}{Incidence\ Power} = \frac{Output\ Signal}{(IR\ Radiance \times Detector\ Sensitive\ Area)} \tag{1.5}$$

Noise Equivalent Power: Noise Equivalent Power (NEP) is the minimum radiant power, which is required to obtain a unity Signal-to-Noise ratio. S/N is equal to output signal voltage divided by detector noise voltage. The definition of the NEP is given below.

$$NEP = \frac{Incidence\ Power}{(S/N)} = \frac{Incidence\ Power}{(V_s\ /V_n)} \tag{1.6}$$

where V_s is the output signal and V_n detector noise. The unit of the NEP is Watts.

Specific Detectivity: Specific detectivity D^* is a very useful parameter for comparing the performance of the detectors with different sizes. The definition of the D^* is given by

$$D^* = \frac{responsivity \times \sqrt{area \times \Delta f}}{noise} = \frac{R\sqrt{A_d \times \Delta f}}{N} \tag{1.7}$$

where Δf is bandwidth. A good detector has a large specific detectivity.

Noise Equivalent Temperature Difference: Noise Equivalent Temperature Difference (NETD) shows the smallest temperature difference which is detected by the detector. NETD is given by [6]

$$NETD = V_n \frac{\Delta T}{\Delta V_s} \tag{1.8}$$

where V_n is the rms noise and ΔV_s is the signal measured for the temperature difference ΔT.

General information about IR radiation and infrared detector types has been presented in this chapter. InSb, InAsSb and HgCdTe detector technologies, and a literature survey on the passivation of InSb based materials will be discussed in the following chapter.

CHAPTER II

InSb, $InAs_{1-x}Sb_x$ and $Hg_{1-x}Cd_xTe$ DETECTOR TECHNOLOGIES

2.1 InSb Detectors

Indium Antimonide (InSb) is III-V compound semiconductor, and it is an important material for the detection of infrared radiation in the 3-5 µm atmospheric window. The cutoff wavelength of InSb is 5.5 µm at 77 K. InSb is a direct bandgap material. It is a narrow bandgap semiconductor with very high electron mobility [7]. Due to its high electron mobility, InSb has received a great deal of attention and has been used in infrared imaging systems, magnetoresistive sensors, high-speed photodetectors and free space communication. InSb based detectors have been available since late fifties [5]. It has strong covalent bonding, and large area InSb wafers are commercially available which make it primary material for MWIR applications.

Bulk growth techniques such as Czochralski and horizontal Bridgman can be used to grow InSb bulk single crystals. Higher quality and more complex InSb based structures can be grown by using epitaxial growth methods such as liquid phase

epitaxy (LPE), molecular beam epitaxy (MBE) and metalorganic chemical vapor deposition (MOCVD) [5].

For device applications, high quality growth of InSb layers on Si or GaAs substrates is desirable [8]. Although, there is a large lattice mismatch between InSb and those materials, there are many reports on the growth of InSb/ Silicon (Si) and InSb/ Gallium Arsenide (GaAs) heterostructures by MBE and MOCVD. In order to reduce the lattice mismatch between the InSb and Si (%19) or GaAs (%14.5), buffer layers are generally used. Growth of InSb layers on Si or GaAs substrates eliminates the need for substrate thinning. Using Si as a substrate provides reduction in the thermal expansion coefficient mismatch between the detector array and Si read-out circuit which increases the reliability of hybrid integration. Some studies made on the InSb detectors are listed below.

Lee *et al.* [9] reported InSb p^+- n layer grown on InSb substrate by MBE. Before growing the detector epilayers, a 300 A^o thick InSb buffer layer was grown by atomic layer epitaxy. Electron mobilities of 65 000 and 125 000 $cm^2V^{-1}s^{-1}$ at room temperature and 77 K were achieved, respectively. The detector structure consisted of a 0.6 μm thick p^+ layer and 5 μm n-layer. Passivation layer of 3000 A° of SiO_2 was deposited by plasma enhanced chemical vapor deposition at 90 °C. The InSb homoepitaxy mesa diodes showed an R_0A value of $2.5x10^5$ Ω-cm^2 at 77 K.

Kimukin *et al.* [10] reported InSb p-i-n photodetectors grown GaAs substrate. Si_3N_4 was used for passivation in this study. I-V characteristics were measured at room and liquid nitrogen temperatures. The dark currents were 20 nA and 6.4 μA at zero bias at 77 K and 300 K, respectively. At 77 K, zero bias-differential resistance area product (R_0A) for 30 μm diameter diodes was 1 Ω-cm^2, and it increased to 2 Ω-cm^2 for 80 μm diameter diodes.

Tevke *et al.* [11] studied dark current analysis and characteristics of InSb p-i-n photodetectors grown on GaAs coated Si substrates by MBE. 400x80 μm^2 mesa

structures were defined by wet chemical etching (1:5 nitric:lactic acid). The ohmic contacts for both n and p – type materials were formed by evaporating TiW/Au and lift-off. Passivation layer was not used in this study. The R_0 at 77 K was approximately 8.3 kΩ and the dark current was 13 μA under a bias voltage of – 0.1 V. The current responsivity and quantum efficiency were around 1.4 A/W and 40%, respectively. The voltage responsivity around 4.5 μm was 1.2×10^4 V/W at 77 K.

Ozer *et al.* [12] studied InSb photodiodes grown on GaAs coated Si substrate by MBE. The structure consisted of a 1.5 μm thick n^+-layer, ~5 μm thick intrinsic layer and a 1 μm thick p^+-layer. The fabricated diodes had an area of 30x30 μm^2 and the peak detectivity at 80 K was $\sim 1 \times 10^{10}$ $cmHz^{1/2}W^{-1}$ (near 4.8 μm) and the quantum efficiency was 50% without antireflection coating. The R_0A product at 80 K of the detectors was limited by ohmic leakage under small reverse bias and trap-assisted-tunneling became dominant as the detector reverse bias approached 0.1 V. The R_0A product was 1 Ω-cm^2 at 80 K.

Michel *et al.* [13] reported InSb photodetectors based on p-i-n structures. Epitaxial layers were grown on 2 μm GaAs coated Si substrates by MBE. The structure consisted of a 1μm thick p-type layer (1×10^{18} cm^{-3}), a 6 μm thick n type active layer (2×10^{15} cm^{-3}), and a 1.5 μm thick n^+ layer (1×10^{18} cm^{-3}). 400x400 μm^2 mesa structures were defined by standard photolithography technique and wet chemical etching. Ti-Au was evaporated for ohmic contacts. There was no passivation layer on these structures. The dark current was 5 mA under a reverse bias of 1.5 V at 77 K. The R_0A product was approximately 1 Ω-cm^2 at 77 K. The maximum voltage responsivity was 1×10^3 V/W around 4 μm at 77 K.

2.2 InAsSb Detectors

Another important material for MWIR applications is Indium Arsenide Antimonide ($InAs_{1-x}Sb_x$) ternary alloy. High quality InAsSb photodetectors for 3-5 μm atmospheric window have been developed during the last 20 years [5]. It is a direct bandgap material and its bandgap can be adjusted by changing antimony mole

fraction (x). The cutoff wavelength of $InAs_{1-x}Sb_x$ detectors is tunable from 3.1 μm (x = 0.0) to 9.0 μm (x ≈ 0.6). It is capable of operating at the longest cutoff wavelength, 9 μm at 77 K, of the entire III-V alloy family. The bandgap of the $InAs_{1-x}Sb_x$ can be described by the following equation [5]

$$E_g(x,T) = 0.411 - \frac{3.4\times10^{-4}T^2}{210+T} - 0876x + 0.70x^2 + 3.4\times10^{-4}xT(1-x) \tag{2.1}$$

where E_g is in eV and T is in K. Cutoff wavelength (λ_c) can be calculated by using $\lambda_c=1.24/E_g$. This equation shows that the bandgap energy of the ternary compound is a square function of x which indicates a weak dependence of the bandgap on composition when compared with mercury cadmium telluride (HgCdTe).

Until 1970s, the main obstacle in the rapid development of InAsSb devices was the problem of the preparation of single crystals and high quality epilayers. The lattice mismatch between InAs and InSb (6.9%) and the large separation between the liquidus and solidus place difficulties in the preparation of single crystals. These difficulties are overcome by using epitaxial techniques. MBE and MOCVD are commonly used growth techniques today which allow growing more sophisticated and quality structures. High quality and lattice matched substrates are required for fabrication of high performance large format InAsSb detector arrays. InAsSb layers can be grown on InSb, InAs and GaSb substrates. Even with the large lattice mismatch, it is very attractive to use GaAs and Si as substrates for InAsSb epitaxial growth. To relieve strain caused by lattice mismatch, buffer layers are grown between the InAsSb layers and the substrate. Higher quality InAsSb layer can be grown on Si substrates by using GaAs buffer layers.

Dobbelaere *et al.* [14] reported the comparison of the performance of $InAs_{0.85}Sb_{0.15}$ infrared photodiodes grown on GaAs, and GaAs coated Si substrate by MBE. The Si substrate was coated with a 4.5 μm thick GaAs buffer layer. A 30 nm thick InAs layer and a 1μm thick linearly graded $InAs_{1-x}Sb_x$ ($0.01<x<0.15$) epilayer were grown on both substrates. It was observed that only a limited number of

dislocations reached the p-n junction for the diodes on GaAs substrate. For the epilayers grown on Si substrate, the dislocation density was higher. Although, the current voltage characteristics were comparable, the diodes on Si substrate had larger leakage currents and lower detectivity because of a higher defect density ($1.5x10^{11}$ cmHz$^{1/2}$W for GaAs and $5x10^{10}$ cmHz$^{1/2}$W for Si substrates at 3.8μm). The R_0A was 192 Ω-cm^2 for InAsSb/GaAs, and 41 Ω-cm^2 for InAsSb/GaAs/Si detectors at 77 K.

Chiang *et al.* [15] reported the first p-n junction formation in $InAs_{1-x}Sb_x$ (0.4<x<0.7) detectors grown on InSb substrate by MOCVD. p^+-n junction were formed by zinc (Zn) diffusion into the undoped n-type epitaxial layer. As an ohmic contact, 800 Aº of indium (In) and 1100 Aº of silver (Ag) were evaporated for both p^+ and n type layers. Epilayer was etched in lactic acid : HNO_3 (8:1) solution to delineate diodes. The I-V measurements were performed at 77 K. The forward and reverse characteristics were affected by the generation-recombination current in the depletion region and by surface leakage current. It is believed that recombination centers in the depletion region were caused by diffusion-induced damages and by lattice mismatch dislocations between the InAsSb epilayer and the InSb substrate.

Kim *et al.* [16] reported the first InAsSb-based long wavelength (8-14 μm) photodiode operating at near room temperature. The epilayers were grown by low pressure MOCVD on GaAs substrate. The structure consisted of a 0.5 μm thick heavily doped InSb p-type (≈$3x10^{18}$ cm^{-3}) contact layer, a 3 μm thick p-type ($3.6x10^{16}$ cm^{-3}) $InAs_{1-x}Sb_x$ absorber layer, and a 2 μm thick n^+-type InSb layer (≈ $3x10^{18}$ cm^{-3}). 400x400 μm^2 devices were fabricated. A room temperature photoresponse of up to 13 μm was obtained in a p^+-InSb/ π-$InAs_{0.15}Sb_{0.85}$/ n^+-InSb heterojunction device. The peak voltage responsivity was $9.13x10^{-2}$ V/W at 300 K and 28.5 V/W at 77 K. Voltage responsivity increased with decreasing temperature, but the increase was much less compared to the calculations. Possible reasons for this are high dark current due to the high doping level in the active area, and the poor interface properties due to lattice mismatch between the absorber and contact

layers. A voltage responsivity-area product of 3×10^{-5} V-cm^2/W was obtained at 300 K for the photodiode optimized for λ= 10.6 μm.

Chakrabarti *et al*. [17] reported homojunction $InAs_{0.96}Sb_{0.04}$ p-i-n photodetectors grown on InAs substrate by LPE. 2.5 μm thick p^+-type layer was doped to 2×10^{18} cm^{-3} with Zn. 4.5 μm thick n-type active layer was unintentionally doped and had residual carrier concentration of 10^{16} cm^{-3}. 380 μm diameter photodiodes were fabricated. Electrical and optical characteristics were performed at room temperature. The dark current of the photodetector was modeled by considering the diffusion, generation-recombination and tunneling currents (trap-assisted tunneling, TAT and band-to-band tunneling, BTB). The results of the fitting study revealed that TAT current was dominant even at low reverse voltage while BTB tunneling became significant at very high reverse voltage. The detectivity was 5.57×10^8 cmHz$^{1/2}$/W at 3.75 μm. It was observed that, in spite of a significant amount of TAT current at reverse bias, the photodiodes exhibited high detectivity at room temperature.

Besikci *et al.* [18] reported the fabrication and characteristics of pin $InAs_{0.8}Sb_{0.2}$ photodetectors grown on GaAs substrate by MBE. The thicknesses of the p and n layers were 300 nm and 4 μm, respectively. The doping of the p layer was 3×10^{18} cm^{-3}, and that of the n layer was 2×10^{18} cm^{-3}. The thickness of the intrinsic layer was 1.5 μm. The fabricated diode had an area of 50x200 μm^2, and the peak detectivity was 1.4×10^{10} cmHz$^{1/2}$/W at 3.9 μm at 80 K. The peak detectivity at 240 K was 7.5×10^8 cmHz$^{1/2}$/W at 4.7 μm. The cutoff wavelengths of the detectors were 4.7 and 5.4 μm at 80 and 240 K, respectively.

Mohammed *et al.* [19] reported $InAs_{0.85}Sb_{0.15}$ photodiodes grown on InAs substrates by LPE. The structure consisted of a 0.5 μm thick undoped n-type layer, and a 0.5 μm thick 5×10^{17} cm^{-3} doped p-type layer. The detectivity of the photodiodes was 2×10^{10} cmHz$^{1/2}$/W at λ=3.5 μm and T=200 K, and it was 1.5×10^{11} cmHz$^{1/2}$/W at 77 K.

2.3 HgCdTe Detectors

$Hg_{1-x}Cd_xTe$ (MCT) is one of the most important semiconductors for infrared detection. It is a direct bandgap material, therefore its absorption coefficient is very high which provides high quantum efficiency. It is a II-VI material, and its cutoff wavelength can be adjusted from 0.7 to 20 μm by changing the CdTe mole fraction (x) [11]. The empirical equation below shows the relationship between the bandgap, Cd mole fraction x and the temperature [5]

$$E_g(x,T) = -0.302 + 1.93x - 0.81x^2 + 0.832x^3 + 5.35(1-2x)10^{-4}\left(\frac{-1822+T^3}{255.2+T^2}\right) \qquad (2.2)$$

where E_g is in eV and T is in K. Cutoff wavelength (λ_c) can be calculated by using $\lambda_c = 1.24/E_g$. Figure 2.1 shows the variation of λ_c with x and temperature.

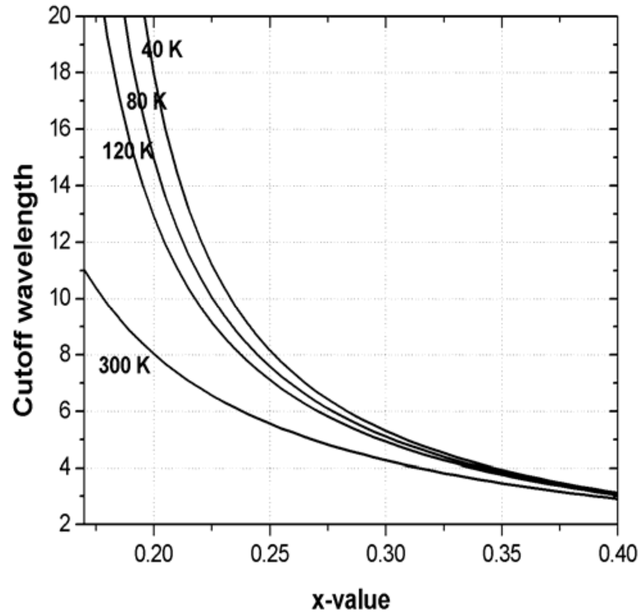

Figure 2.1: Cutoff wavelength versus CdTe mole fraction

It is inferred that, small variations in the composition result in large change in the cutoff wavelength in the LWIR and VLWIR regions. Hence, to ensure composition uniformity across the large area LWIR wafers is very difficult.

Bulk and epitaxial growth techniques such as LPE, MBE, MOCVD and chemical vapor deposition (CVD) are used to grow HgCdTe [5]. Low temperatures are required for epitaxial growth techniques compared to bulk growth techniques. Epitaxial growth methods allow growing high quality and multilayer structures. Growing high quality epilayers depends on the availability of good quality lattice matched substrates to the HgCdTe. Cadmium Zinc Telluride (CdZnTe) is lattice matched to HgCdTe, and it is transparent in the MWIR and LWIR atmospheric windows. However, high quality large area CdZnTe substrates are not available. Also, they exhibit low mechanical strengths, and there is a large thermal expansion coefficient mismatch between the Si read out integrated circuit (ROIC) and CdZnTe. HgCdTe can be grown on alternate substrates such as Si, sapphire, GaAs, InSb and germanium (Ge) [20]. Buffer layers must be grown on alternate substrates to reduce the lattice mismatch between the HgCdTe and the substrates. Si substrates are widely used. They are available in large sizes up to 8 inches, and they are mechanically strong. There is no thermal expansion coefficient mismatch between the Si read-out circuit and Si substrate which provides long term thermal cycle reliability. However, the lack of suitable buffer layer results in high defect density which reduces the performance of the detectors.

2.4 Passivation Techniques used for InSb Based Materials

The surface passivation is very important for the focal plane arrays based on narrow bandgap semiconductors. It is important to use a passivation layer to protect photodiodes from the ambient conditions and to reduce the surface leakage. The passivation layers should be chemically protective as well as electrically insulating. A low temperature passivation is required in order to prevent damage to the semiconductor material.

Gong *et al.* [21] studied sulphur passivation of LPE grown mid-infrared InAsSb layers on InAs substrate. Mesas having diameter of 0.4 mm were fabricated. I-V characteristics were measured under -0.5 V at 300 K and 77 K before and after

sulphur treatments. Samples were dipped in ammonia sulphide solution at room temperature for several ten minutes. After passivation, the dark current was changed from 0.18 mA to 20 nA at 77 K, and it was decreased almost three times at 300 K. This significant reduction of the dark current after passivation was due to the reduction of surface recombination.

Sun *et al.* [22] studied the effect of different passivation processes on the current – voltage characteristics of the InSb p^+-n diodes. They deposited third gate electrode to study the surface effect on the I-V characteristics of a p-n junction. Either an anodic oxide plus a photo-CVD SiO_2 double layer or a photo-CVD SiO_2 single layer was used as a passivation layer in this study. Measurements were done at 77 K. The I-V characteristics of a diode passivated by a combination of 400-500 A^o thick anodic oxide and 1500 A^o thick SiO_2, were almost independent of the gate voltage. The I-V characteristics of a diode passivated by single photo-CVD SiO_2 layer showed strong dependence of the gate voltage which indicated that the reverse leakage current was flowing through the surface region.

Bloom *et al.* [23] presented improved surface passivation for gate controlled, backside illuminated InSb photodiodes fabricated on thinned n-type InSb wafer. The carrier concentration of n-type region was $1\text{-}1.6\times10^{15}$ cm^{-3}, and p^+ junction were formed by berilium implantation. For surface passivation, they used photo-assisted SiO_x deposition (PHOTOX). The electrical performance of photodiodes at optimum gate bias (up to 1 V reverse bias) with small geometries junctions (30x30 μm^2) was the same as that observed in large junctions, indicating that the performance was limited by the properties of starting bulk material rather than the passivation of frontside, where the junctions were implanted. The R_0A product of diodes with junction area of 9×10^{-6} cm^2 was 5×10^4 Ω-cm^2 at 77 K.

Clahorra *et al.* [24] studied a method for passivation of InSb by vacuum deposition of SiO_x. For this study, n type InSb layers with donor concentrations in the range of 0.9×10^{14}-2.2×10^{14} cm^{-3} were used. Two groups of samples were prepared. The first

group included air-exposed samples, on which 70 nm thick SiO_x films were evaporated. The second group included samples with 20-50 nm thick anodic oxide and 70 nm thick SiO_x multilayer passivation. Au-Cr electrodes were evaporated on SiO films and unoxidized parts of the InSb layers for capacitance-voltage (C-V) measurements. The C-V measurements were performed at 77K. They observed that the fixed charge density was $1x10^{12}$ cm^{-2}, and the trap density was $8x10^{11}$ cm^{-2} for the sample including single layer passivation, and these values decreased to $2x10^{11}$ cm^{-2}, and to $4x10^{11}$ cm^{-2} for the samples including multilayer passivation, respectively. They concluded that directly evaporated SiO_x is not an adequate passivation layer on InSb, and buffer layer is needed.

Bregman *et al*. [25] studied the effects of heat treatments on the chemical properties of InSb metal-oxide-semiconductor structures prepared by wet anodization and plasma oxidation. n-type InSb samples with donor concentration ranging from $0.9x10^{14}$ to $2.2x10^{14}$ cm^{-3} were used in this study. The wet anodization was performed using a PH-5 acid-glycol-water (AGW) solution. The plasma oxidation was done under 50 mTorr oxygen pressure and constant current conditions. The annealing was carried out in dry nitrogen (N_2) atmosphere for 1 h at 80 C° and 250 C° for wet-anodic oxide and up to 285 C° for plasma-grown oxides. After the heat treatments, oxide traps and fast interface state densities decreased for both oxidation methods. On the other hand, the fixed oxide charge density increased for the sample coated with wet anodic oxide, and decreased for the sample coated with plasma oxide with heat treatments.

Wu *et al.* [26] investigated the sulphur passivation effects on InGaAsSb/GaSb photodiodes. P^+-InGaAsSb/N-InGaAsSb structure was grown on GaSb substrate by MOCVD. 400x400 μm^2 area photodiodes were fabricated. The I-V characteristics of the fabricated diodes were measured at room temperature, then the sulphur treatment was made by using $(NH_4)_2S$: H_2O (1:4) solution at 50 ºC for 10 min. I-V characteristics were measured again. Treatment steps were repeated and I-V characteristics were measured up to nine times. It was observed that the dark current decreased with the increase of the passivation process time. The dark

current changed from 62 to 1.6 μA at 0.1 V reverse bias, and the zero bias resistance R_0 was changed from 2.2 kΩ to 82 kΩ after 90 min sulphur treatment. In order to investigate the stability of the structure after the sulphur passivation, the I-V characteristic of the sample was measured immediately after it was passivated for 30 min. Then after 80-day exposure to ambient environment, the I-V characteristic was measured again, and a little performance improvement was observed. It can be concluded that the sulphur treatment improves the performance of InGaAsSb photodiodes and the resulting passivation layer is robust and durable.

Zhang *et al*. [27] studied the effects of alkali and neutralized $(NH_4)_2S$ passivation on the performance of MBE grown InGaAsSb pin photodetectors. Two samples were prepared from the same epitaxial wafers to compare the effects of different sulphure passivation solutions. The devices were fabricated by standard photolithography and wet chemical etching techniques. The mesa sizes were 400x400 μm^2. Two samples were dipped into alkali $(NH_4)_2S$ solution (0.5 M, pH=11) and neutralized $(NH_4)_2S$ solution, which was neutralized by hydrochloric acid until pH=7 respectively at 60 ºC for 1 h. The I-V measurements were made before and after sulphur treatment at room temperature. The dark current density decreased from 1.01 mA/cm^2 to 490 $\mu A/cm^2$ for the alkali solution treatment and to 87 $\mu A/cm^2$ for the neutralized solution treatment at 0.5 V reverse bias, respectively. Devices passivated by neutralized solution showed better performance than the ones passivated by alkali solution. It can be concluded that neutralized $(NH_4)_2S$ solution is more effective sulphur passivation method for InGaAsSb detectors.

This chapter has discussed InSb, HgCdTe and InAsSb detector technologies. Literature survey on the passivation studies made by other research groups on InSb based detectors have also been given in this chapter. Surface passivation is one of the most important factors in limiting device performance. In this study, the effect of two different passivation layers on the performance of InAsSb based detectors was investigated. A combination of a sulphur and polyimide and a single layer polyimide were used as passivation films in this study. In order to observe the effect of different passivation layers and to investigate the contributions of the

surface and bulk components to the total dark current, the dark currents of detectors with different dimensions will be analyzed in Chapter IV. Test detector fabrication, electrical and optical characterizations and noise current analysis will be presented in the next chapter. The epilayer structures utilized in this work will also be described in the following chapter.

CHAPTER III

TEST DETECTOR FABRICATION AND ELECTRICAL CHARACTERIZATION

3.1 Epilayer Structures Used For Test Detector Fabrication

Two different structures were used in this study. The first structure (Figure 3.1(a)) is a homojunction $InAs_{1-x}Sb_x$ photodetector which was grown by MBE on GaAs substrate at Interuniversity Micro-Electronics Center (IMEC), Belgium. The targeted Sb mole fraction was 0.6. However, optical characteristic results revealed that Sb mole fraction was ~0.13 and the cut-off wavelength was around 4.1 µm. The doping level and the thickness of the n^+ layer are 3 x 10^{18} cm^{-3} and 0.5 µm, respectively. This structure also includes a 250 nm thick graded doped n layer, 250 nm thick 5 x 10^{16} doped n^- layer, and 5 x 10^{16} doped p^- layer. The thickness of the 2 x 10^{18} cm^{-3} doped bottom p^+ layer is 3.6 µm. The thin top contact layer provides low series resistance. The doping concentration of the active layer should be low to reduce tunneling dark current. For high quantum efficiency, the p^+ layer should be doped as high as possible.

(a)
n^+ $InAs_{1-x}Sb_x$ (0.5 μm)
n $InAs_{1-x}Sb_x$ (0.25 μm)
n^- $InAs_{1-x}Sb_x$ (0.25 μm)
p^- $InAs_{1-x}Sb_x$ (1.8 μm)
p^+ $InAs_{1-x}Sb_x$ (3.6 μm)
GaAs Substrate

(b)
p^+ $InAs_{0.8}Sb_{0.2}$ (300 nm)
intrinsic (1.5 μm)
n^+ $InAs_{0.8}Sb_{0.2}$ (400 nm)
GaAs Substrate

Figure 3.1: Epilayer structures : (a) structure 1, (b) structure 2.

The second structure (Figure 3.1 (b)) includes a 300 nm thick p^+ $InAs_{0.8}Sb_{0.2}$ layer, 1.5 μm thick intrinsic layer and 400 nm thick $InAs_{0.8}Sb_{0.2}$ n^+ layer. The doping levels are 3 x 10^{18} and 2 x 10^{18} cm^{-3} for p^+ and n^+ layers, respectively. The epilayer was grown on GaAs substrate. This sample was also grown by MBE on GaAs substrate at Interuniversity Micro-Electronics Center (IMEC).

3.2 Test Detector Fabrication

In order to investigate the effects of different passivation layers on the performance of the InAsSb based photodetectors, variable area test detectors were fabricated. Detectors with different periphery/area ratios allow revealing the contributions of the surface and bulk currents to the total detector dark current. Same fabrication steps were applied to both structures. The fabrication process included the following steps:

- Mesa etch
- Metallization
- Passivation
- Fan-out metallization

The test detector mask used for the fabrication has three identical regions, which allow comparison of the effect of the three different passivation layers (Figure 3.2).

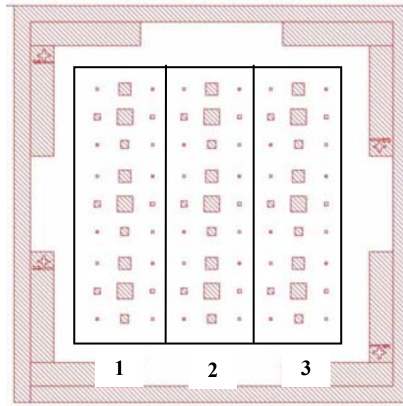

Figure 3.2: Mesa mask.

Photolithography and wet chemical etching were made to define the mesa patterns. Both structures were etched in Citric acid: H_2O_2 (1:1) solution. The etching solution was kept at 30 ºC and stirred at 250 rpm in order to obtain uniform etch throughout the sample. $InAs_{1-x}Sb_x$/GaAs layer was etched down to bottom p^+ layer, and $InAs_{0.8}Sb_{0.2}$/GaAs layer was etched down to bottom n^+ layer. The picture of the etched surfaces taken by an optical microscope is given in Figure 3.3 (a). Each sample contained detectors with different dimensions: 200x200 μm^2, 150x150 μm^2, 100x100 μm^2, 75x75 μm^2, 50x50 μm^2 and 33x33 μm^2.

After etching, contacts were formed by metal deposition and lift-off (Figure 3.3 (b)). A double layer of titanium (Ti) and gold (Au) were evaporated in order to make contacts to p and n materials.

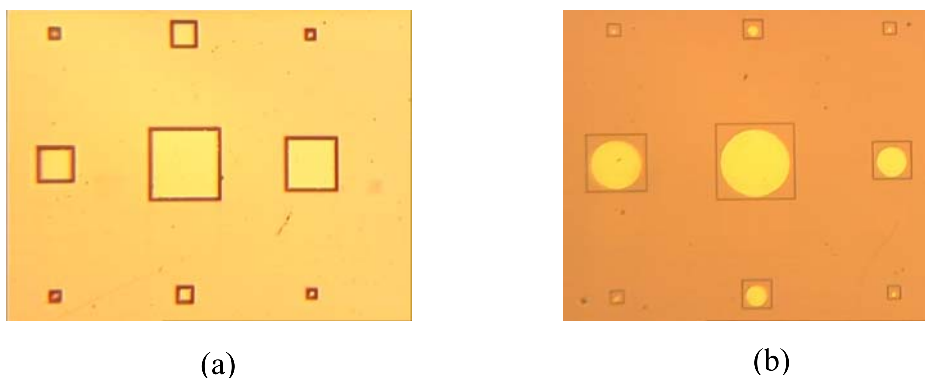

(a) (b)

Figure 3.3: (a) The picture of mesa structures, (b) mesas with Ti/Au ohmic contacts.

Metallization process was followed by the passivation of the layers. Three different layers were used in this work. Number labels 1, 2 and 3 in Figure 3.2 show the sample areas on which different passivation layers were applied. Single layer polyimide was applied to region 1. Sulphur treatment and polyimide were applied to region 2. Sulphur treatment, silicon dioxide (SiO_2) and polyimide were applied to region 3. For sulphur treatment, photolithography was made to mask the region 1, and contact places of regions 2 and 3. Treatment was made by dipping the samples into ammonia sulphide $(NH_4)_2S$ solution for ~ 10 minutes at room temperature. After the treatment, samples were rinsed in deionized water and dried with nitrogen. This process was followed by coating of the whole surfaces of both structures with polyimide, and photolithography was performed to remove the polyimide from region 3, and to open the contact places in regions 1 and 2. Unwanted polyimide layers were etched in developer, and hard bake of the polyimide-coated samples was performed on the hot plate. So, passivation process of regions 1 and 2 was completed. Before silicon dioxide (SiO_2) deposition, photoligraphy was made to mask regions 1 and 2, and contact places in region 3. About 600 nm SiO_2 layer was deposited by sputtering, and unwanted SiO_2 layers were removed by lift-off technique. To complete the passivation of region 3, silicon dioxide layers were coated with polyimide, and hard bake was performed on the hot plate.

After the passivation process, Ti and Au were evaporated in order to make fan-out lines and metal pads (Figure 3.4).

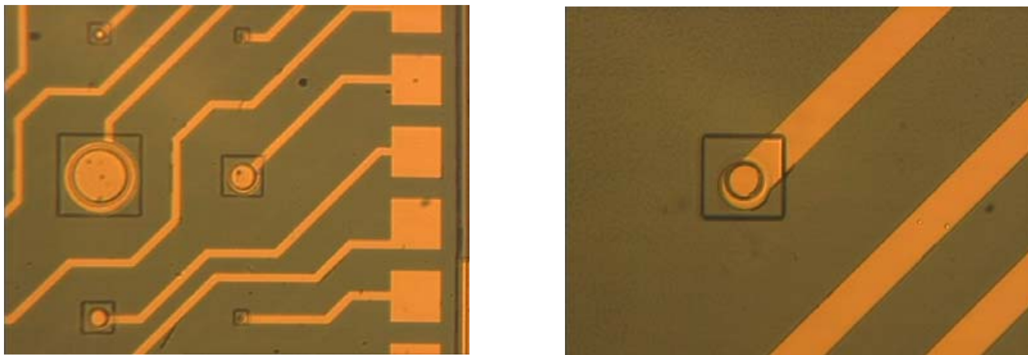

Figure 3.4: Picture of the sample with fan-out metallization.

Finally, for characterization, samples were mounted on an alumina substrate with a thermal compound, and electrical contacts were taken by wire bonding. Figure 3.5 shows the picture of the sample mounted on an alumina substrate.

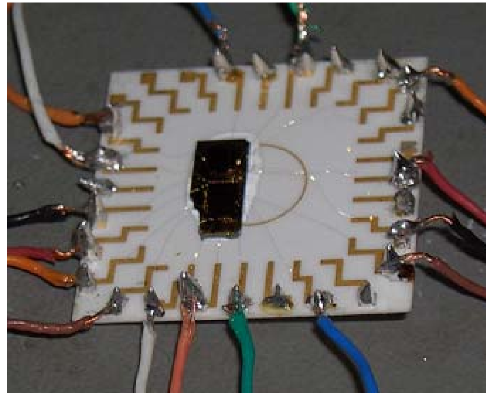

Figure 3.5: Structure 1 mounted on an alumina substrate.

3.3 Characterization of the Test Detectors

This section presents the electrical and optical characterizations and noise current analysis of the test detectors fabricated by using the epilayer structures described in the first section. The I-V characteristics were measured by using Keithley 238 source-measure unit under computer control at 77 K. Measurement setup is given in Figure 3.6.

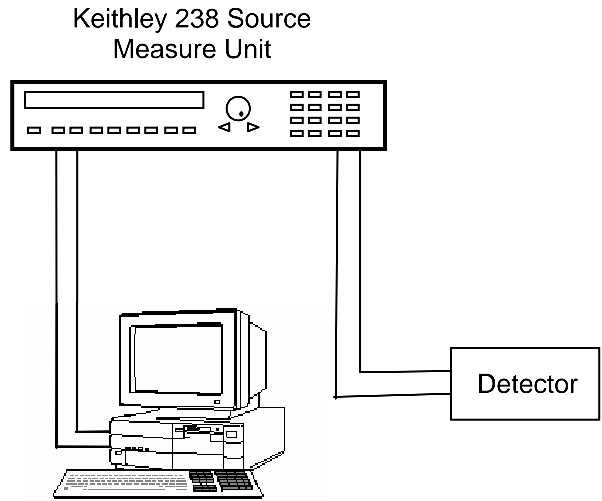

Figure 3.6: I-V measurement setup.

The spectral response of the detectors was measured by using Oriel MIR-8000 FTIR system. The block diagram of the responsivity and detectivity measurement set up is given in Figure 3.7. The blackbody radiation is modulated by the chopper, and the detector signal is amplified by preamplifier. The amplified signal is fed into a lock-in amplifier, which is locked to the chopper frequency.

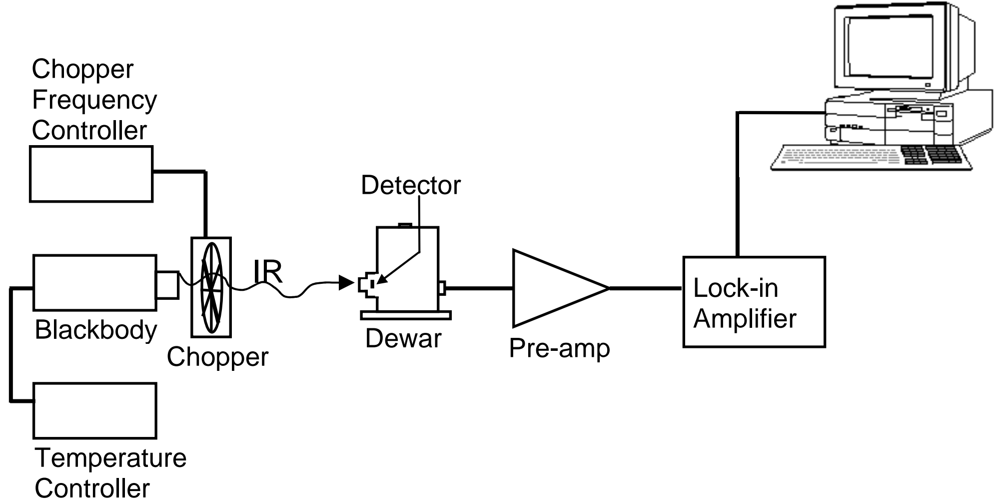

Figure 3.7: Block diagram of the set up used for responsivity and detectivity measurement [28].

Agilent 4395A spectrum analyzer was used for noise measurements. Detectors were placed in a liquid-nitrogen dewar. Low noise preamplifier was used to amplify noise signals.

3.3.1 Characterization of $InAs_{1-x}Sb_x$ Detector

3.3.1.1 Electrical Characteristics

Detailed electrical characterization was made in order to identify the dominant dark current mechanisms. I–V measurements were taken at 77 K under zero illumination. Because of the problems with the fabrication process, diodes passivated with a combination of polyimide, SiO_2 and sulphur layers showed linear characteristics. The I-V characteristics of the double layer passivated diodes with variable perimeter/area ratios are shown in Figure 3.8.

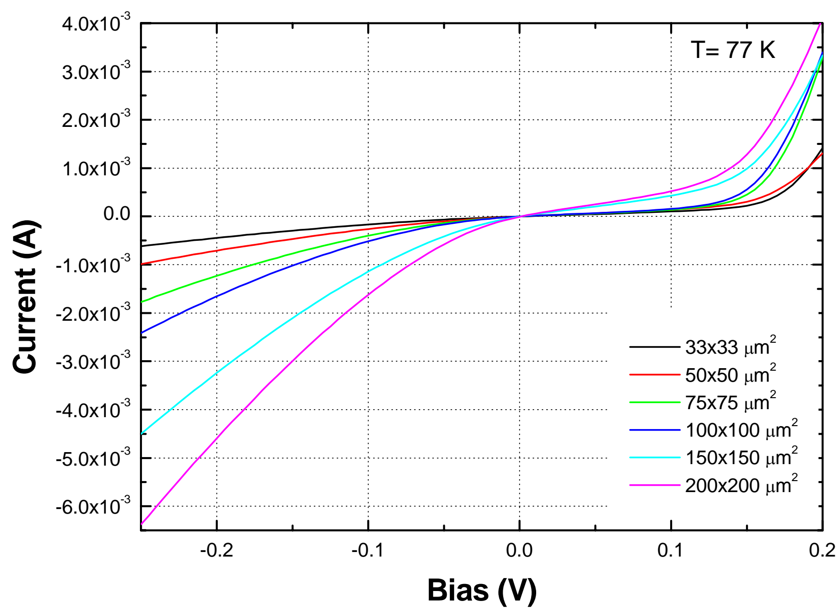

Figure 3.8: The I-V characteristics of the detectors with different areas.

In an ideal diode, the zero-bias resistance area product (R_0A) is independent of perimeter-area ratio of the diode. The R_DA-V characteristics of 33x33 μm^2, 50x50

μm^2, 75x75 μm^2, 100x100 μm^2 and 200x200 μm^2 detectors passivated by a polyimide are shown in Figure 3.9. It is seen from the figure that the R_0A product decreases with decreasing diode area. This dependence on diode dimension suggests that smaller area diode is more dependent on perimeter or surface effects than the larger area diode. Perimeter related effects are therefore likely to decrease R_0A product with decreasing diode area. The zero-bias resistance area product of the polyimide coated 33x33 μm^2 detector is 0.011 Ω-cm^2 at 77 K.

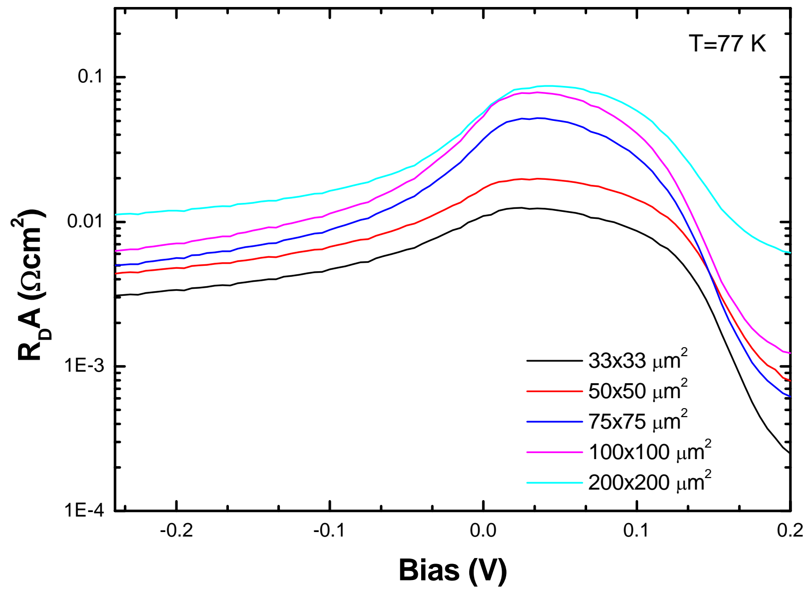

Figure 3.9: R_DA-V characteristics of 33x33 μm^2, 50x50 μm^2, 75x75 μm^2, 100x100 μm^2, and 200x200 μm^2 detectors (region 1).

3.3.1.2 Optical Characteristics

The optical characteristics were performed for the backside illuminated polyimide coated 33x33 μm^2 detector at 80 K. Figure 3.10 shows the spectral response of the detector. The experimental cut-off wavelength (% 50 response) is ~4.1 μm, which is not in agreement with the targeted Sb mole fraction of 0.6. The targeted cut-off wavelength of this material was about 9 μm at 80 K.

Epilayers grown on lattice mismatched substrates have higher dislocation density than that of the epilayers grown on lattice matched substrates. The high lattice mismatch between the InAsSb epilayer and the GaAs substrate induces high recombination centers close to the substrate which are associated with the dislocations. For backside illuminated detectors, most of the higher energy photons are absorbed close to the substrate, which leads to a sharp reduction of the spectral response with decreasing wavelength as can be seen from Figure 3.10. This observation is similar to that of Johnson *et al.* [34] for HgCdTe detectors.
It is also seen from Fig. 3.10 that the spectral responsivity does not decrease sharply at the cutoff wavelength. This is probably due to the interaction of electrons with photons which have energy lower than the bandgap due to intermediate states.

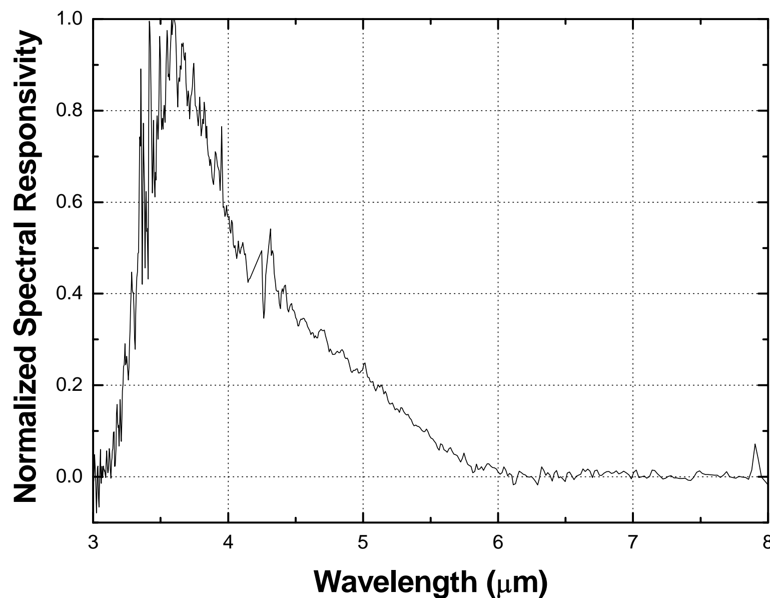

Figure 3.10: Normalized spectral responsivity versus wavelength.

Detectivity and responsivity measurements were carried out by backside illumination and without anti-reflection coating. The blackbody source was set at 500 ºC, and the chopper at 675 Hz. The bias was kept around zero during the measurements. The measured peak detectivity was ~3.65×10^{10} cmHz$^{1/2}$/W at 3.58 μm. Since this epilayer is grown on the lattice mismatch GaAs substrate, the

detectivity is an order of magnitude lower than that of the MWIR detectors grown on lattice matched substrate [19]. It can be increased by improving the material quality and optimizing the epilayer structure.

3.3.1.3 Noise Current Analysis

The noise current spectral density was measured in the 0-6.4 kHz range under reverse bias voltages at 80 K. The measurement results are given in Figure 3.11. 1/*f* noise is observed in the low frequency range, and it increases with the reverse bias voltage.

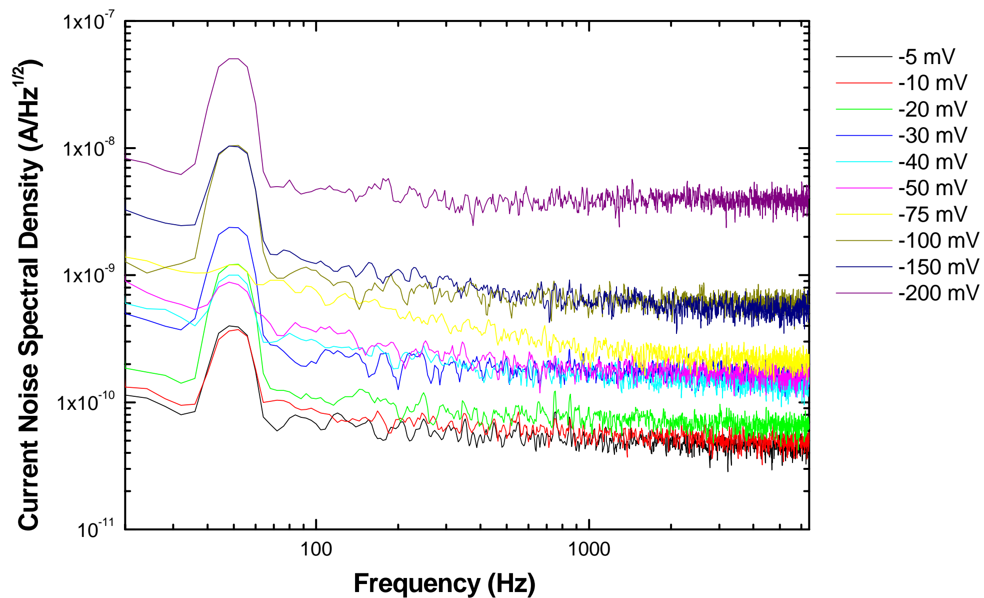

Figure 3.11: Noise current spectral density as a function of frequency under reverse bias voltages.

The 1/*f* noise current correlates with one of the mechanisms that generate the dark current. As presented in the following chapter, trap-assisted tunneling (TAT) mechanism is the dominant dark current component at 80 K. The correlation between the 1/*f* noise current and the TAT current can be expressed as [29]

$$i_n = \alpha_{TAT} (I_{TAT})^{\beta} \tag{3.1}$$

where I_{TAT} is the trap-assisted tunneling current. This equation is fit to the measured results. The 1/*f* noise current of the detector at 1 Hz is obtained by using noise current spectral density. The variation of noise current spectral density at 1 Hz with the detector current and the fitting result are shown in Figure 3.12. α_{TAT} and β values are obtained as $4.2\text{x}10^{-7}$ and 0.61, respectively. These values are close to those found by Nemirovsky and Unikovsky for HgCdTe photodiodes ($\alpha_{TAT} \cong 1\text{x}10^{-6}$ and $\beta \cong 0.5$) [29].

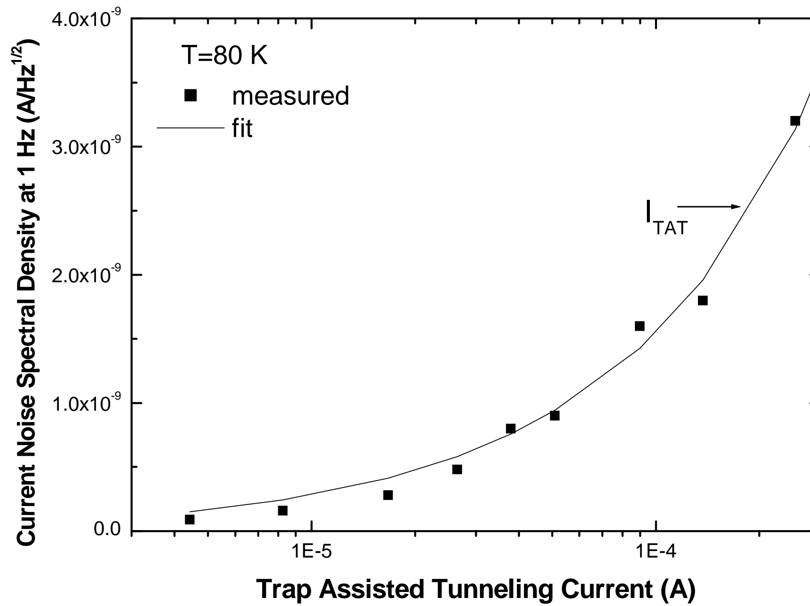

Figure 3.12: The variation of 1/*f* noise as a function detector dark current at 80 K.

3.3.2 Characterization of $InAs_{0.8}Sb_{0.2}$ Detector

3.3.2.1 Electrical Characteristics

The I-V characteristics of 33x33 μm^2 $InAs_{0.8}Sb_{0.2}$ diodes with different passivation layers at 77 K are shown in Figure 3.13. As can be seen from the figure, the dark current is lower for the detector with double layer passivation than that of the detector with single layer passivation. Comparison of the passivation layers will be presented in the next chapter.

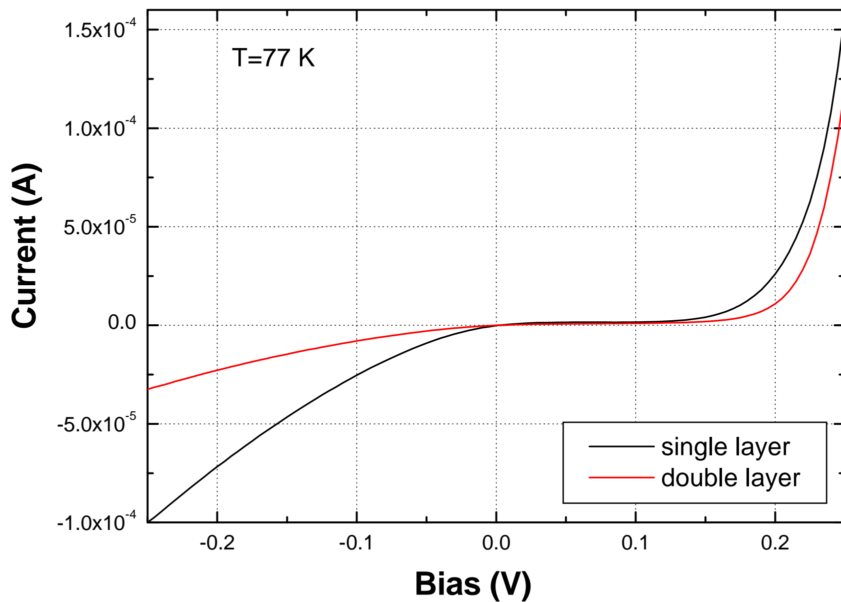

Figure 3.13: I-V characteristics of the diode passivated with different layers. The red and black lines represent the I-V characteristics of the diode passivated by a combination of sulphur and polyimide and single layer polyimide, respectively.

Figure 3.14 shows the I-V characteristics of 33x33 μm^2, 50x50 μm^2, 75x75 μm^2, 100x100 μm^2, 150x150 μm^2 and 200x200 μm^2 area detectors (region 2), respectively. The variation of the resistance-area products with reverse bias voltage for these detectors is given in Figure 3.15. It is seen from the figure that the R_DA values show little area dependence which indicates reduced surface current

contribution to the total dark current. The zero-bias differential resistance-area product of double layer passivated 33x33 μm² detector is 0.53 Ω-cm² at 77 K.

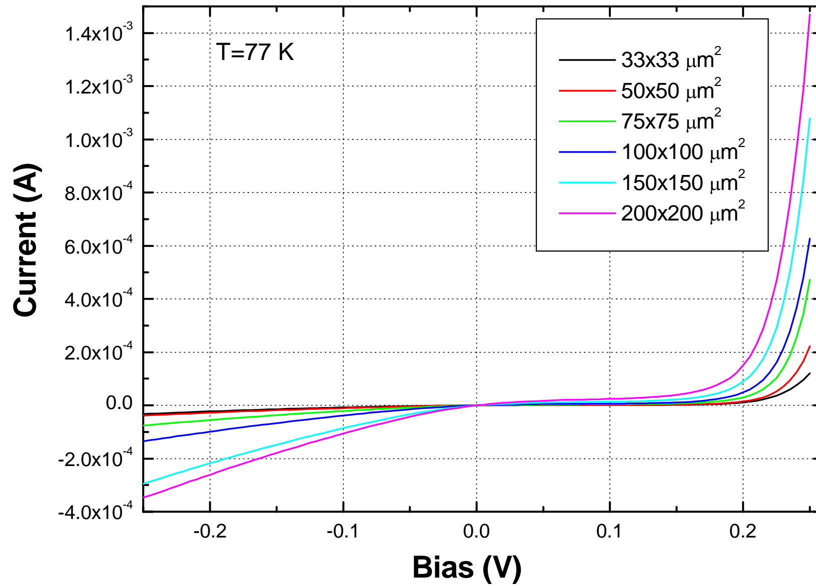

Figure 3.14: The I-V characteristics of the detectors with different areas.

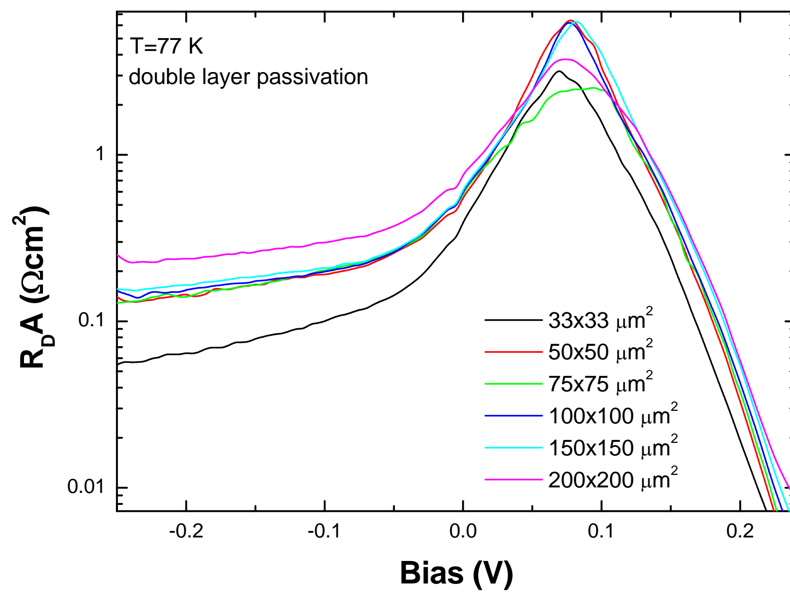

Figure 3.15: R_DA-V characteristics of 33x33 μm², 50x50 μm², 75x75 μm², 100x100 μm², 150x150 μm² and 200x200 μm² detectors (region 2).

3.3.2.2 Optical Characteristics

The spectral response of a backside illuminated 33x33 μm^2 $InAs_{0.8}Sb_{0.2}/GaAs$ detector coated with double layer passivation is shown in Figure 3.16. It is seen from the figure that the spectral responsivity decreases rapidly for photons with energy higher than the bandgap of the semiconductor. The rapid reduction of the spectral response with decreasing wavelength is due to high recombination centers close to the substrate where most of the higher energy photons are absorbed. The high recombination centers are related to the high lattice mismatch between the InAsSb epilayer and the GaAs substrate. The peak detectivity is ~1.22×10^{10} $cmHz^{1/2}/W$ at 80 K. The peak detectivity is lower than that of the detectors grown on lattice matched substrates.

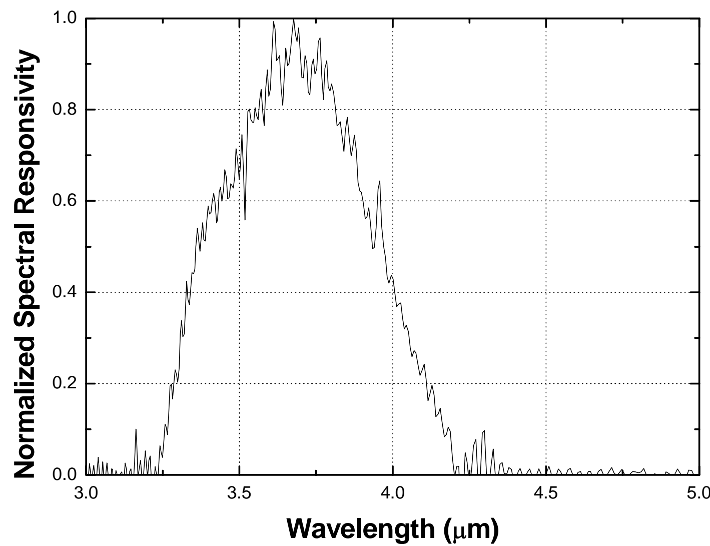

Figure 3.16: Normalized spectral responsivity versus wavelength.

3.3.2.3 Noise Current Analysis

Noise measurements were performed under reverse bias voltages at 80 K. The measurement results are given in Figure 3.17. An empirical relationship between the $1/f$ noise current and the trap-assisted- tunneling current was given in Equation

3.1. When this equation is fit to the measured results, α_{TAT} and β values were obtained as 9x10^{-7} and 0.56, respectively. Figure 3.18 shows the fitting results. Obtained α_{TAT} and β values are close to those found by Nemirovsky and Unikovsky for HgCdTe detectors ($\alpha_{TAT} \cong$ 1x10^{-6} and $\beta \cong 0.5$) [29].

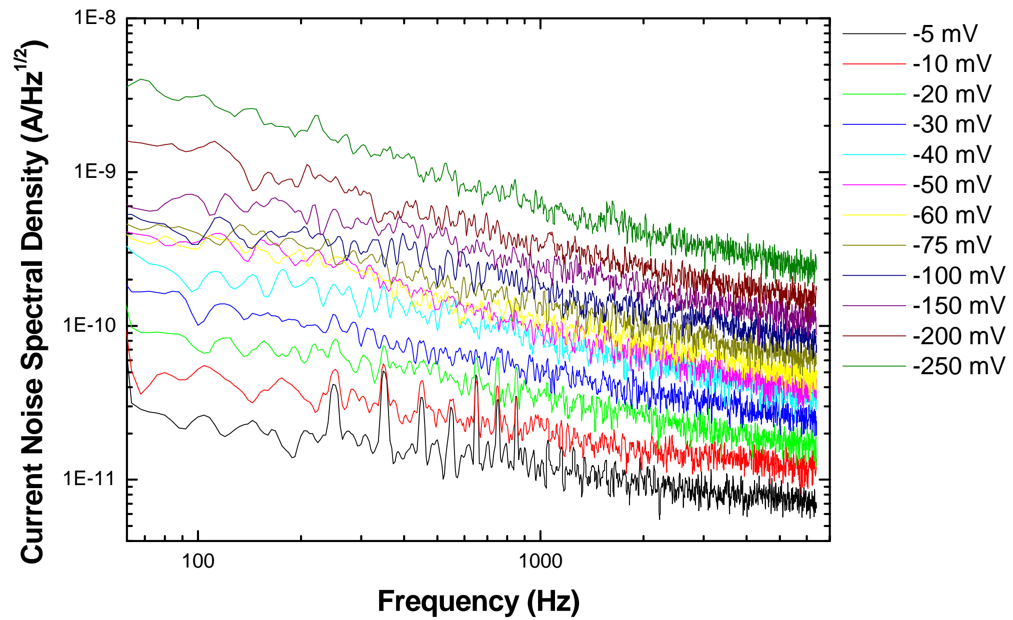

Figure 3.17: Noise current spectral density as a function of frequency under reverse bias voltages.

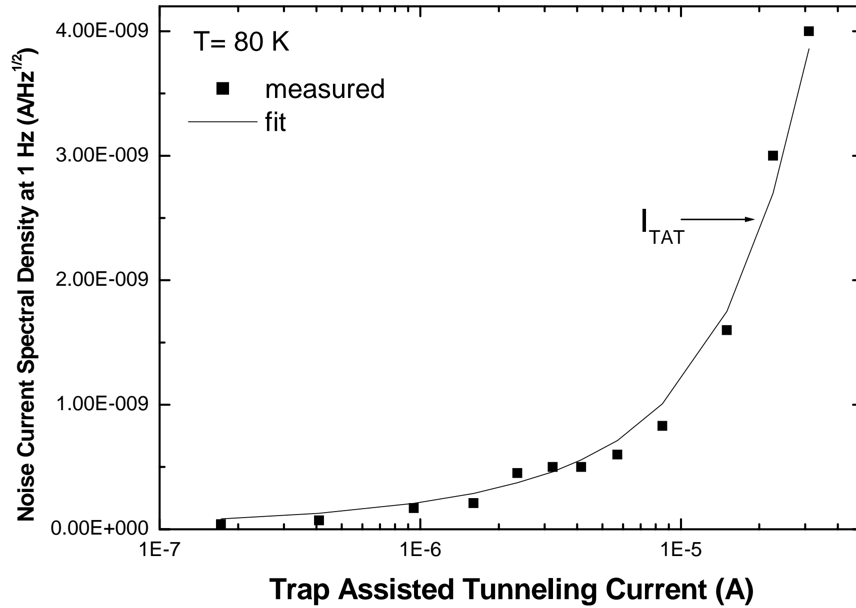

Figure 3.18: The variation of 1/*f* noise as a function detector dark current at 80 K.

This chapter has discussed the fabrication of the variable area test detectors and their electrical and optical characterizations. Noise current analysis was also performed in order to understand the correlation between the 1/*f* noise current and the dark current mechanisms. It was observed that, the 1/*f* noise current at 1 Hz was related to the trap-assisted tunneling current at 80 K for both epilayer structures. A large lattice mismatch between the epilayer and the substrate introduces additional traps to the material which increases the TAT and 1/*f* noise current. Therefore, a reduction in the trap density is needed to get higher performance detectors. Detailed dark current analysis will be presented in the following chapter.

CHAPTER IV

DARK CURRENT MODELLING

4.1 Dark Current Analysis

It is important to determine the dominant dark current mechanisms limiting the detector performance. Usually one current mechanism is dominant over the others, depending on the operating temperature and the bias. Once the dominant dark current mechanisms are found, the performance of the photodiodes can be enhanced by improving the fabrication process, material growth conditions or epilayer structure design. Surface, bulk or depletion region can contribute to the dark current of the photodiode. Each of the dark current generation mechanisms has its own individual relationship to voltage and temperature. The dominant dark current mechanisms in the corresponding bias and temperature regions can be identified by fitting the measured differential resistance values to the theoretical formulations. The basic components of the dark current and the fitting procedure of theoretical models to the measured results are presented in the following sections.

4.1.1 Diffusion Current

Diffusion current results from the diffusion of thermally generated minority carriers

from the neutral n and p-regions to the other side of the junction. It is a fundamental dark current mechanism. It occurs in the bulk region of the diode. Diffusion current density can be defined as [5]

$$J_D = J_s\left[\exp\left(\frac{qV}{kT}\right) - 1\right] \tag{4.1}$$

where q is the electron charge, V is the applied bias, k is the Boltzmann constant, T is the diode temperature, and J_s is the saturation current density given by [5]

$$J_s = q\left[\frac{D_n n_p}{L_p} + \frac{D_p p_n}{L_n}\right] \tag{4.2}$$

where D_n and D_p are the minority carrier diffusion constants in cm^2/s, L_n and L_p are the minority carrier diffusion lengths in cm for electrons and holes respectively. n_p and p_n are the electron and hole minority carrier concentrations in cm^{-3}. Using the relations below

$$D = \mu\frac{kT}{q} \tag{4.3}$$

$$n_i^2 = n_n p_p \tag{4.4}$$

$$L = \sqrt{\tau D} \tag{4.5}$$

J_s can be rewritten as

$$J_s = n_i^2 (qkT)^{1/2}\left[\frac{1}{p_p}\left(\frac{\mu_n}{\tau_n}\right)^{1/2} + \frac{1}{n_n}\left(\frac{\mu_p}{\tau_p}\right)^{1/2}\right]^{-1} \tag{4.6}$$

where n_i is the intrinsic carrier concentration, and μ_n, μ_p are electron and hole mobilities respectively. τ_n and τ_p are electron and hole life-times in the p and n type regions, respectively. Diffusion current varies with n_i^2 which depends on the temperature. Therefore, it is the dominant dark current mechanisms at higher temperatures. The associated dynamic resistance is given by

$$(R_{DIFF})^{-1} = C_{DIFF} \exp\left(-\frac{qV}{kT}\right) \tag{4.7}$$

$$C_{DIFF} = \frac{kT}{qAJ_S} \tag{4.8}$$

where C_{DIFF} is bias independent fitting parameter, and A is the detector area.

4.1.2 Generation-Recombination Current

There are several generation-recombination (g-r) mechanisms in narrow bandgap semiconductors. This mechanism occurs either at the surface or in the depletion region. Shockley-Read-Hall (SRH) centers within the depletion region may be present in the original material or these may be created during the fabrication processes. Therefore, these centers can be lowered with optimization of the growth or processing conditions. The g-r centers localized at the surface can be reduced by surface passivation. Generation-recombination current density can be given as [5]

$$J_{g-r} = \left(\frac{n_i W_o kT}{V_{bi}(\tau_e \tau_h)^{1/2}} + \frac{Ps_o n_i W_o kt}{AV_{bi}}\right)\left(\frac{2\sinh\left(\frac{qV}{2kT}\right)}{\left(\frac{V_{bi}-V}{V_{bi}}\right)^{1/2}}\right) f(b) \tag{4.9}$$

where W_o is the zero bias depletion layer width and V_{bi} is the built-in potential. τ_e and τ_h are the carrier lifetimes of electrons and holes respectively. s_o is the surface

recombination velocity, and V is the applied bias. P and A are the perimeter and the area of the diode, respectively. $f(b)$ is given by [5]

$$f(b) = \int_0^\infty \frac{du}{u^2 + 2bu + 1} \tag{4.10}$$

where

$$b = \exp\left(-\frac{qV}{2kT}\right)\cosh\left(\frac{E_t - E_i}{kT} + \frac{1}{2}\ln\left(\frac{\tau_e}{\tau_h}\right)\right) \tag{4.11}$$

E_i and E_t intrinsic and trapping energy levels, respectively. The associated dynamic resistance is given by

$$(R_{GR})^{-1} = \frac{1}{C_{GR}} \frac{\partial f(V,T)}{\partial V} \tag{4.12}$$

$$f(V,T) = \left(\frac{2\sinh\left(\frac{qV}{2kT}\right)}{\left(\frac{V_b - V}{V_b}\right)^{1/2}} \right) f(b) \tag{4.13}$$

$$\frac{1}{C_{GR}} = A\left(\frac{n_i w_o kT}{V_b \tau_o} + \frac{P s_o n_i w_o kT}{A V_b}\right) \tag{4.14}$$

where C_{GR} is bias independent fitting parameter.

4.1.3 Tunneling Current

Tunneling current can be due to band-to-band tunneling (BTB) and trap-assisted tunneling (TAT). Band-to-band tunneling (BTB) results from the direct tunneling of electrons from the valance band of the p-type region to the conduction band of the n-type region. It contributes to the reverse bias characteristics especially in narrow bandgap semiconductors at relatively high reverse bias voltages. A simple expression for BTB current can be given as [30]

$$J_{BTB} = \frac{q}{4\hbar\pi^2}\left[\frac{E_g kT}{P^2}\right]^{1/2} \int_{-E_{\max}}^{0} T_p\left(\frac{E}{2}\right)dE \tag{4.15}$$

where, P is the momentum matrix, and $E_{\max} = -qV + E_F$. In the above expression, T_P is the tunneling probability given by

$$T_P = \exp\left[-\left(\frac{2m_e}{\hbar^2}\right)^{1/2}\left(\frac{2\varepsilon_0\varepsilon_s}{q^2 N_d}\right)^{1/2} E_g\left\{\left(1-\frac{E}{E_g}\right)\left[\frac{\pi}{2}-\sin^{-1}\left(\frac{-E}{E_g-E}\right)^{1/2}\right]-\left(-\frac{E}{E_g}\right)^{1/2}\right\}\right] \tag{4.16}$$

Trap-assisted-tunneling can occur due to tunneling of minority carriers from the occupied trap states located either in the depletion region or in the quasi-neutral side to the empty band states on the other side of the junction. Trap-assisted tunneling can be given as is [31]

$$J_{TAT} = qN_t\left[\frac{c_p p_1 w N_c}{c_p p_1 + w N_c}\right]x_d \tag{4.17}$$

where N_t is the trap density, c_p is the capture coefficient of holes, $p_1 = N_v \exp\left[-\frac{E_t}{kT}\right]$, N_v is the density of states in the valence band, E_t is the trap energy level, wN_c is the tunneling rate, and x_d is the depletion layer width.. The trap-assisted tunneling current can be formed from thermal and tunneling mechanisms. If it is assumed that the trap-assisted tunneling is limited by tunneling from trap level, in this case

$$c_p p_1 >> wN_c \tag{4.18}$$

Then, the TAT current density can be expressed as

$$J_{TAT} = qN_t (wN_c) x_d \tag{4.19}$$

The tunneling rate is

$$wN_c = \frac{\pi^2 q m_e^* E M^2}{h^3 (E_g - E_t)} \exp\left[-\frac{4(2m_e^*)^{1/2}(E_g - E_t)^{3/2}}{3\hbar qE}\right] \tag{4.20}$$

where m_e^* is the effective mass of electrons, M is the matrix element of the trap potential, and E is the electric field associated with the tunneling barrier. The associated dynamic resistance is given by

$$(R_{TAT})^{-1} = C_{TAT1} \exp\left(\frac{C_{TAT2}}{(V_b - V)^{1/2}}\right)\left(1 - \frac{C_{TAT2}}{2(V_b - V)^{1/2}}\right) \tag{4.21}$$

$$C_{TAT1} = \frac{q^2 A \pi^2 m_v M^2}{h^3 (E_g - E_t)} N_t \tag{4.22}$$

$$C_{TAT2} = -\frac{4(2m_v)^{1/2}(E_g - E_t)^{3/2}}{3q\hbar\left(\frac{qN_d}{2\varepsilon}\right)^{1/2}} \tag{4.23}$$

where C_{TAT1} and C_{TAT2} are bias independent fitting parameters.

4.1.4 Ohmic Leakage Current

The surface leakage currents and the dislocations in the material which intersect the junction are possible sources of ohmic leakage current. Ohmic current is given by [30]

$$I_{sh} = \frac{V}{R_{sh}} \tag{4.24}$$

where V is the applied voltage across the junction, and R_{sh} is the diode shunt resistance.

4.1.5 Dark Current Modelling of $InAs_{1-x}Sb_x/GaAs$ Detector

The dark current modeling was performed for the polyimide coated 33x33 μm^2 detector at 77 K.

The material parameters used for the fitting study were obtained from the equations given below [32, 33] and are given in Table 4.1.

$$n_i = \left(1.35 + 8.5x + 4.22\times10^{-3}T - 1.53\times10^{-3}xT - 6.73x^2\right)\times10^{14}T^{3/2}E_g^{3/4}\exp\left(-\frac{qE_g}{2kT}\right) \tag{4.25}$$

$$V_b = \frac{kT}{q} \ln\left(\frac{N_A N_D}{n_i^2}\right) \quad (4.26)$$

$$\varepsilon_s = 15.15 + 1.65x \quad (4.27)$$

Table 4.1: Material parameters used for $InAs_{1-x}Sb_x/GaAs$ detector at 77 K.

E_g (eV)	V_b (V)	n_i (cm^{-3})	ε_s (F/m)	w_0 (μm)
0.3049	0.29977	7.896×10^{6}	1.36×10^{-10}	2×10^{-6}

In this table, E_g is the energy bandgap, V_b is the built-in potential, n_i is the intrinsic carrier concentration, ε_s is the static dielectric constant, and w_0 is the depletion region width.

In order to identify the dominant dark current mechanisms under various bias voltages at 77 K, the R_D expressions for diffusion, generation-recombination, trap-assisted tunneling and ohmic leakage mechanisms were used. The total differential resistance can be considered as the parallel combination of all resistance components, and it can be expressed as

$$\frac{1}{R_D} = \frac{1}{R_{DIFF}} + \frac{1}{R_{GR}} + \frac{1}{R_{TAT}} + \frac{1}{R_{SHUNT}} \quad (4.28)$$

Equation (4.28) was fit to the measured data under various bias voltages at 77 K. The fitting results are given in Figure 4.1. It can clearly be seen that there is a good agreement between the measured results and fitting. Shunt and trap-assisted tunneling mechanisms are dominant throughout the entire reverse bias range at 77 K. The possible reason for the high level of shunt current is the high level of surface leakage current which is due to a non-ideal surface passivation. The high level of trap-assisted tunneling current indicates a large number of trap levels in the

material. Under small forward bias, generation-recombination current starts to contribute to the dark current.

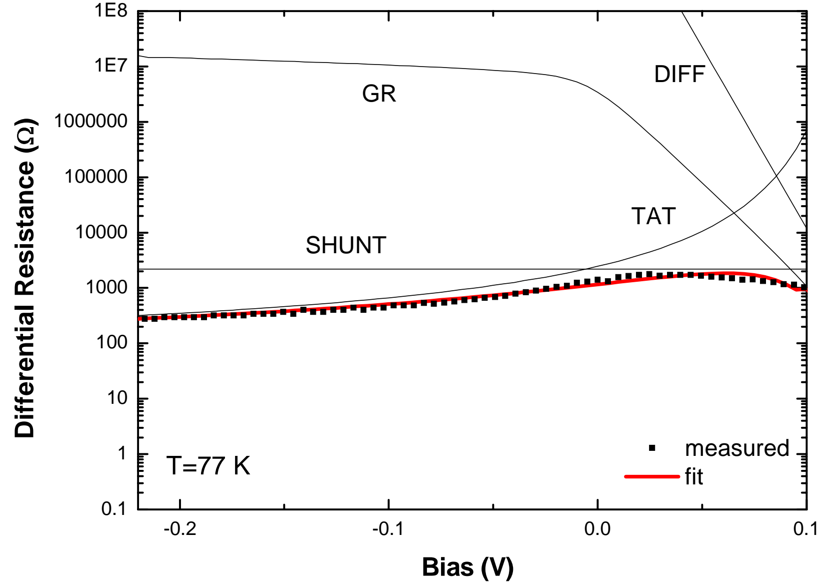

Figure 4.1: The measured and calculated differential resistance of 33x33 μm^2 $InAs_{1-x}Sb_x$ diode passivated by a single layer polyimide (region 1) at 77 K.

Surface and bulk contributions to the diode current are assessed by using variable area diode test structures. The dark current of the detector can be expressed as

$$I_D = P \times J_P + A \times J_A \tag{4.29}$$

$$\frac{I_D}{P} = J_P + \frac{A}{P} \times J_A \tag{4.30}$$

where P is the perimeter of the diode, J_P is the surface current density, A is the area of the diode, and J_A is the bulk current density. J_A can be obtained by fitting the plot of I_D/P versus A/P to Equation (4.30) under different reverse bias voltages. Figures 4.2 and 4.3 show the fitting results of the detectors with single layer and double

layer passivation, respectively. Once J_A is obtained by using Figures 4.2 and 4.3, J_P can be calculated from Equation (4.30).

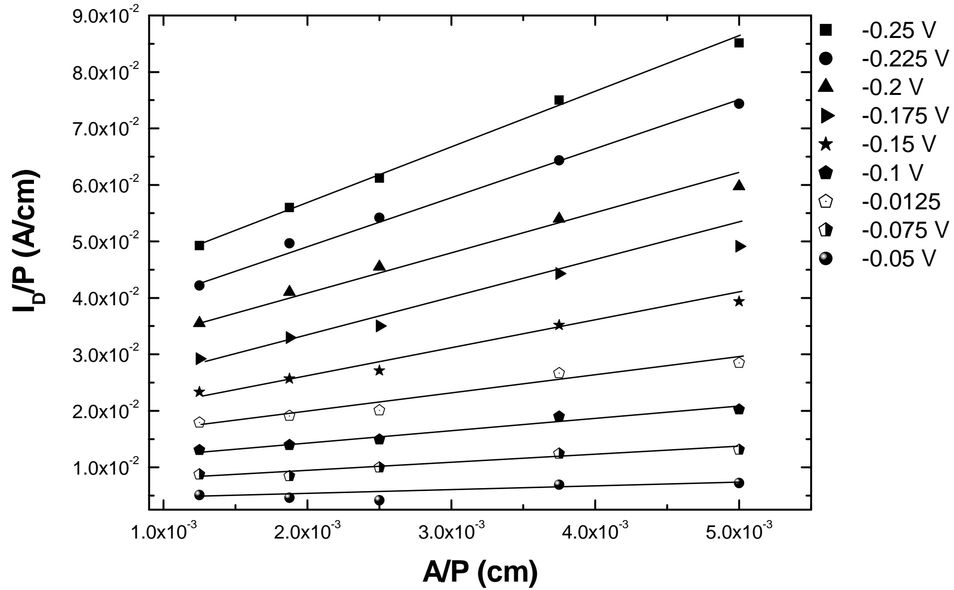

Figure 4.2: Fitting results of polyimide coated detectors. Solid lines represent the fitting results and symbols represent measured data.

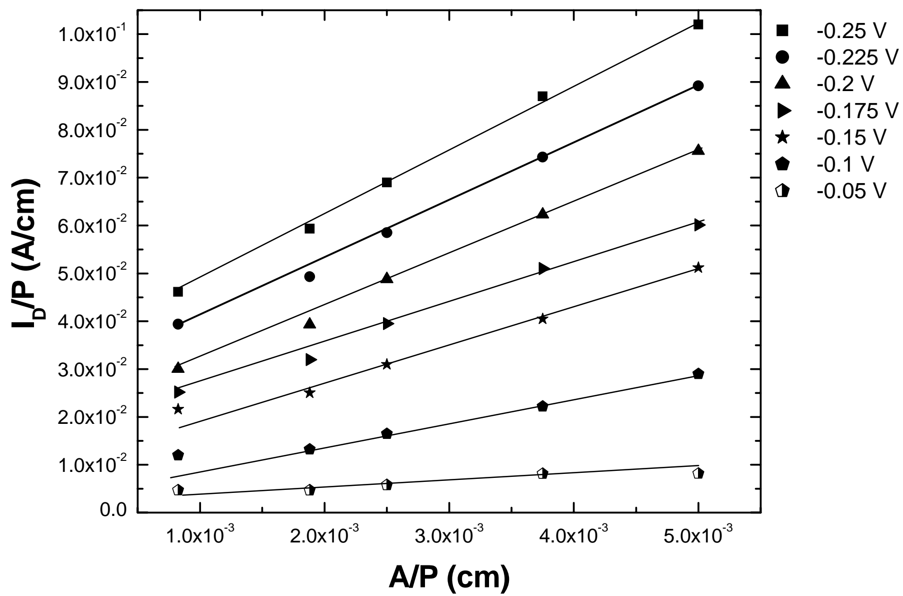

Figure 4.3: Fitting results of the detectors coated with sulphur and polyimide. Solid lines represent the fitting results and symbols represent measured data.

Figures 4.4 and 4.5 show the contributions of the surface and bulk currents to the total dark current for the single and double layer passivated detectors, respectively. As can be seen from Figure 4.4, the dark current is dominated totally by the surface mechanism in the voltage range shown, and surface contribution does not show voltage dependence for single layer passivated diodes. For double layer passivated diodes, it is seen from Figure 4.5 that under small reverse bias voltages dark current is mainly dominated by the bulk mechanisms for detector sizes of 75x75 μm^2, 100x100 μm^2, 150x150 μm^2, and 200x200 μm^2. The bulk mechanism is related with the bulk properties of the epilayer structure such as defect density. The large lattice mismatch between the InAsSb and GaAs substrate may cause the high defect density. The bulk mechanisms can be reduced by improving the material quality. For 33x33 μm^2 detectors, surface current is dominant throughout the entire reverse bias. It is also seen from the figure that the surface contribution increases with reverse bias voltages for all detectors. This is probability due to increased surface tunneling current with reverse bias. The surface contribution increases with decreasing detector dimension as can be seen from both Figures 4.4 and 4.5 which suggests that the smaller area diodes are more dependent on perimeter or surface effects than the larger area diodes, as expected.

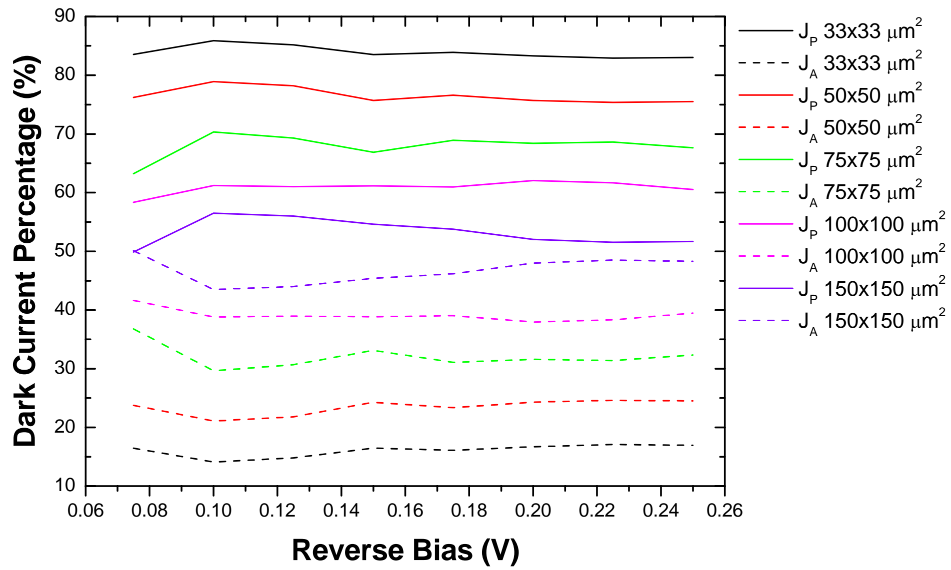

Figure 4.4: Contributions of the surface and bulk currents to the total dark current for different sizes detector (single layer). The dashed lines indicate the bulk, and solid lines indicate the surface components.

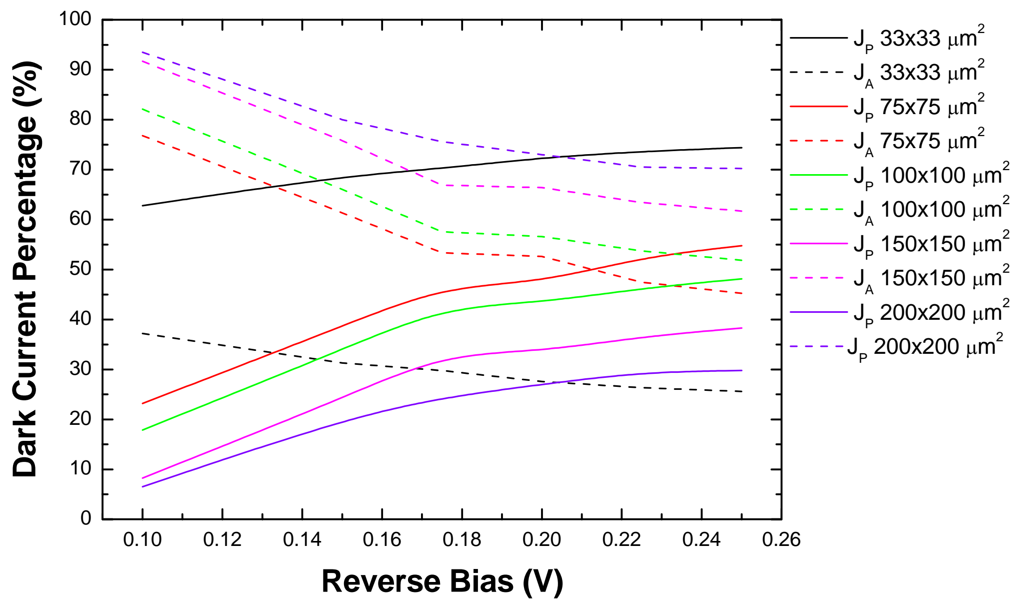

Figure 4.5: Contributions of the surface and bulk currents to the total dark current for different sizes detectors (double layer). The dashed lines indicate the bulk, and the solid lines indicate the surface components.

The contribution of the surface and bulk currents are plotted in the same graph for 33x33 μm² diodes with different passivation layers, in order to investigate the effects of these layers (Figure 4.6). As can be seen from the figure, the surface effects for the detectors passivated by a combination of sulphur and polyimide are lower than those in the detectors passivated by a polyimide. After sulphur treatment, surface recombination process is suppressed due to the termination of the dangling bonds by sulphur atoms. This is the possible reason for the decrease of the surface leakage current in the double layer passivated detector. However, there are high levels of surface current in both diodes. The high levels of surface current indicate insufficient surface passivation, therefore the duration of the sulphur treatment can be increased or different passivation layers may be investigated to improve the device performance.

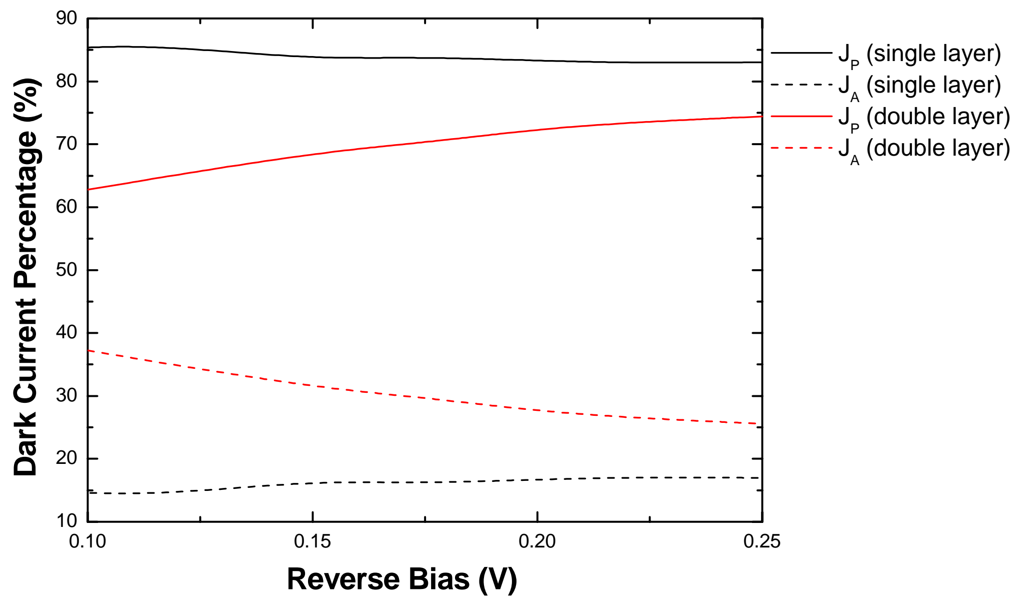

Figure 4.6: Contributions of the surface and bulk currents to the total dark current for detector size of 33x33 μm². The red and black lines indicate single and double layer passivation, respectively. The dashed lines indicate the bulk, and the solid lines indicate the surface components.

4.1.6 Dark Current Modeling of $InAs_{0.8}Sb_{0.2}$/GaAs Detector

The fitting process was performed for the 33x33 $InAs_{0.8}Sb_{0.2}$ μm^2 diode with double layer passivation (region 2) at 77 K. The material parameters used for the fitting study are given in Table 4.2.

Table 4.2: Material parameters used for $InAs_{0.8}Sb_{0.2}$/GaAs detector at 77 K.

E_g (eV)	**V_b (V)**	**n_i (cm^{-3})**	**ε_s (F/m)**	**w_0 (μm)**
0.2610	0.307087	2.2301×10^{8}	1.37×10^{-10}	1.5×10^{-6}

where E_g is the energy bandgap, V_b is the built-in potential, n_i is the intrinsic carrier concentration, ε_s is the static dielectric constant, and w_0 is the depletion region width.

The R_D expression (Equation 4.28) including diffusion, generation-recombination, trap-assisted tunneling and ohmic leakage mechanisms were used for the fitting process Equation 4.28 was fit to the measured data under various bias voltages at 77 K, and the fitting results are given in Figure 4.7. It is seen from the figure that the dynamic resistance is limited by shunt and trap-assisted tunneling currents throughout the entire reverse bias and under small forward bias voltages. Under small forward bias, generation-recombination and diffusion currents start to contribute to dark current.

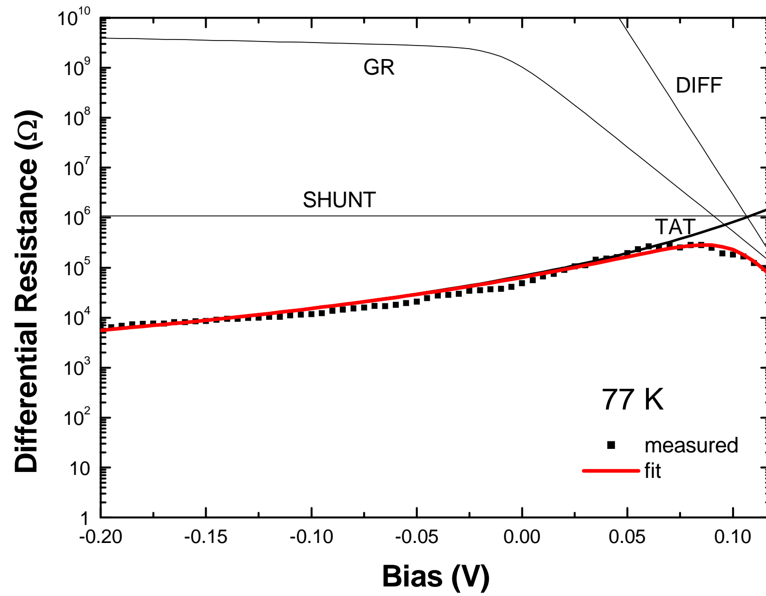

Figure 4.7: The fitting result of 33x33 μm^2 $InAs_{0.8}Sb_{0.2}$ diode with double layer passivation (region 2) at 77 K.

Detectors with different perimeter/area ratios were analyzed at 77 K, in order to investigate bulk and surface contributions to the total dark current. J_P and J_A were obtained by fitting the plot of I_D/P versus A/P to Equation (4.30) under different reverse bias voltages. The fitting results of the diodes with single layer and double layer passivations are shown in Figures 4.8 and 4.9, respectively. Bulk current densities were obtained from these figures and surface current densities were obtained by using Equation (4.30).

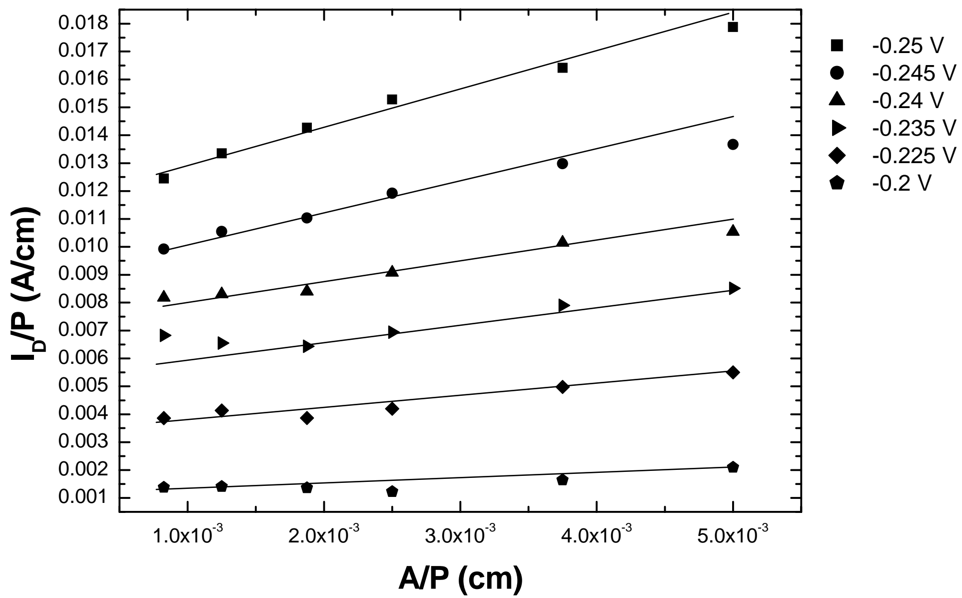

Figure 4.8: Fitting results of polyimide coated detectors. Solid lines represent the fitting results and symbols represent measured data.

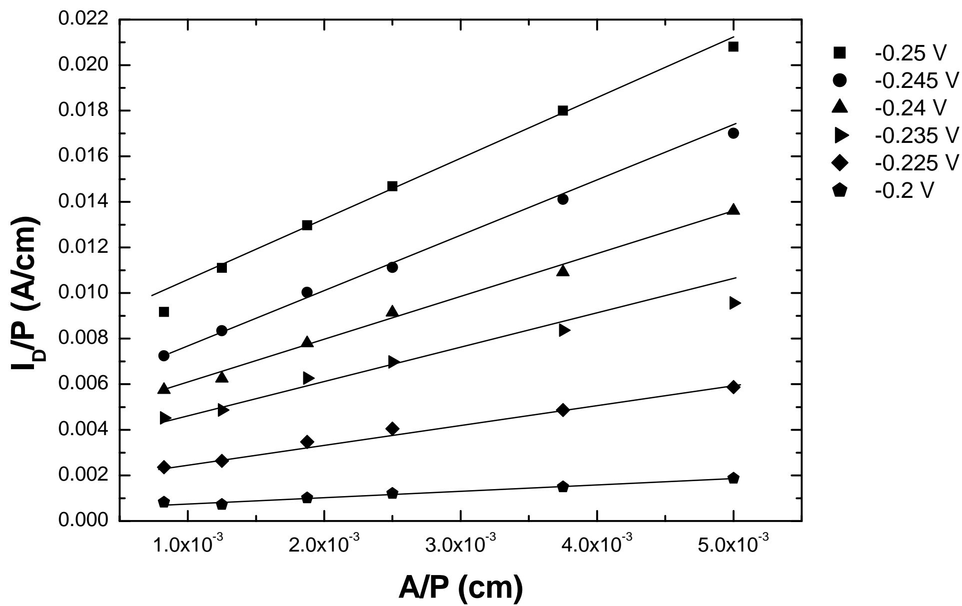

F
igure 4.9: Fitting results of the detectors coated with sulphur and polyimide. Solid lines represent the fitting results and symbols represent measured data.

Surface and bulk current contributions to the dark current are shown in Figures 4.10 and 4.11 for the single layer passivated detectors. It is seen from Figure 4.10 that, for single layer passivated diodes, the dark currents of the detectors are totally dominated by the surface current, and its contribution starts to decrease and bulk current contribution increases when reverse bias voltage approaches 0.245 V. Although other explanations may be possible, this increase in the bulk current conntribution can be attributed to the onset of band to band tunneling. As can be seen from Figure 4.11, the surface current starts to be dominant when reverse bias voltages approaches ≈0.2 V for 150x150 μm^2 and 200x200 μm^2 diodes. These two figures confirm the increasing contribution of the perimeter dependent surface current as the detector size is decreased.

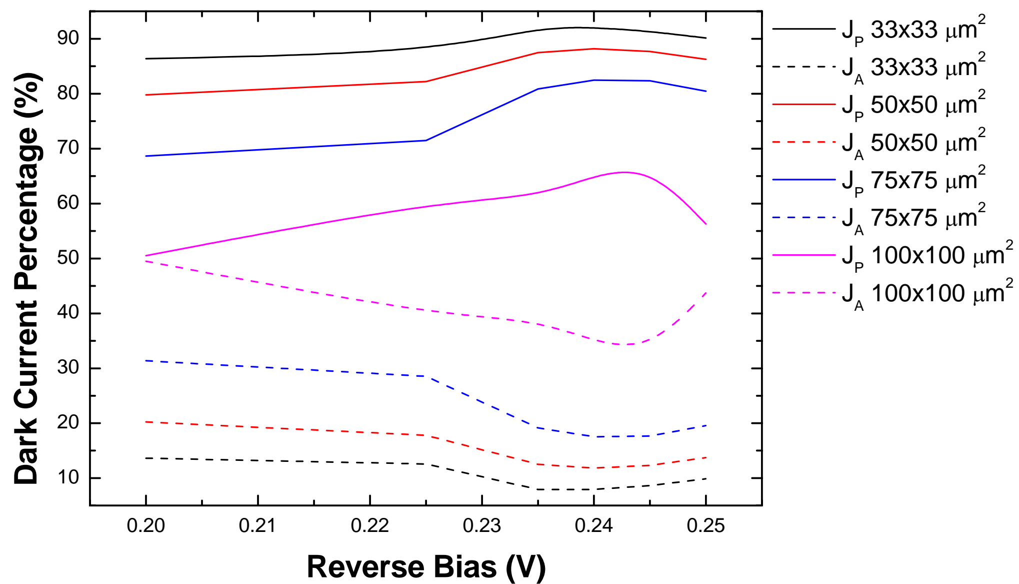

Figure 4.10: Contributions of the surface and bulk currents to the total dark current for different sizes detector (single layer). The dashed lines indicate the bulk, and solid lines indicate the surface components.

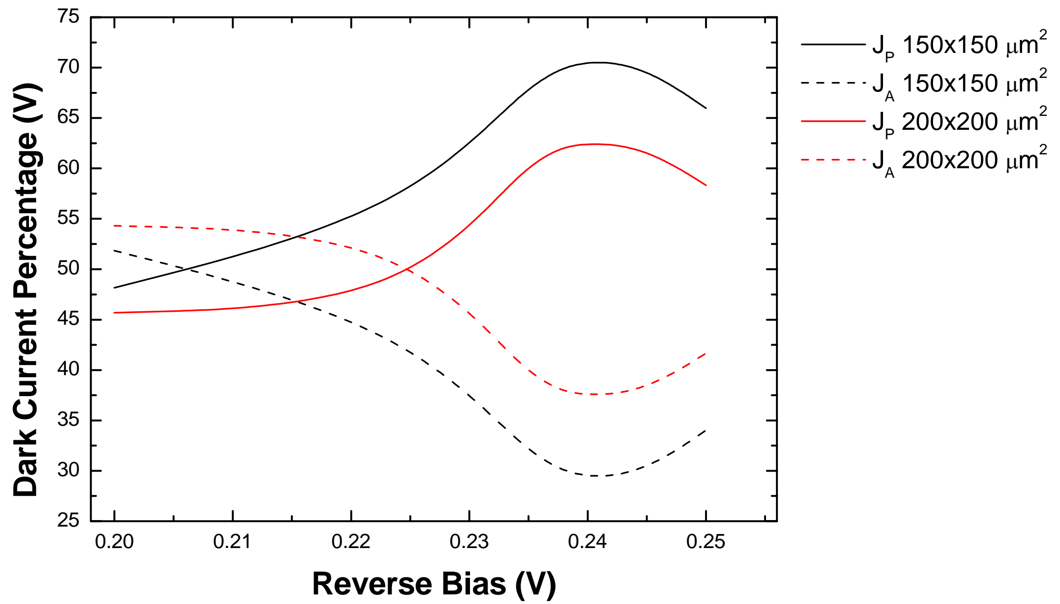

Figure 4.11: Contributions of the surface and bulk currents to the total dark current for 150x150 μm^2 and 200x200 μm^2 detectors (single layer). The dashed lines indicate the bulk, and solid lines indicate the surface components.

The contribution of the surface and bulk mechanisms for the detectors with double layer passivation are shown in Figures 4.12 and 4.13 which display a similar trend.

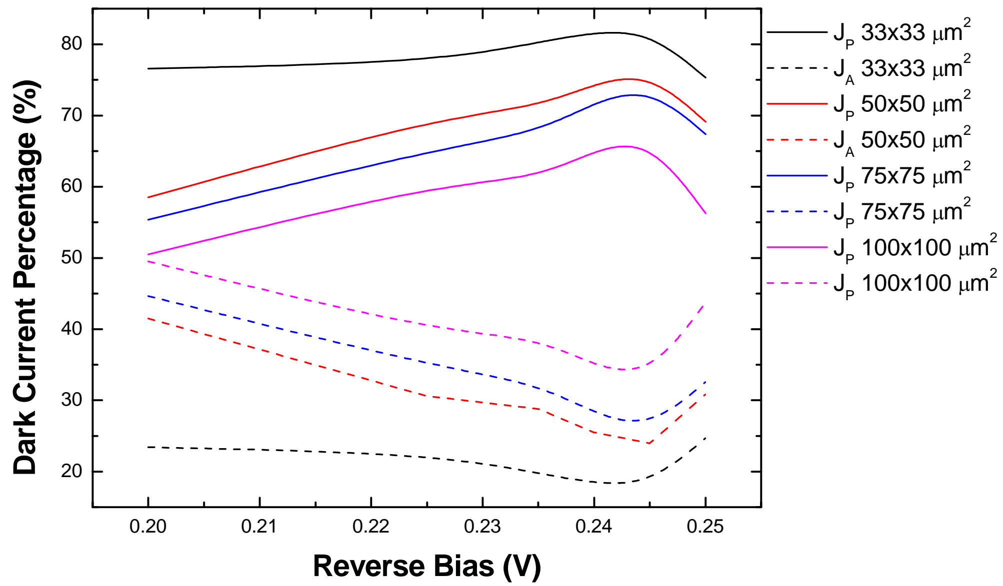

Figure 4.12: Contributions of the surface and bulk currents to the total dark current of the detectors with double layer passivation. The dashed lines indicate the bulk, and solid lines indicate the surface components.

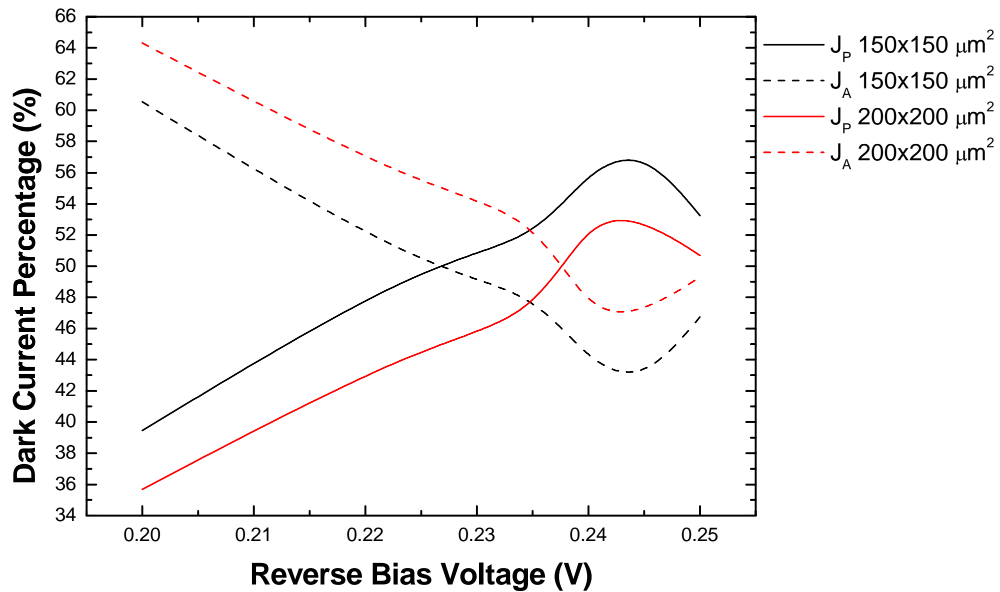

Figure 4.13: Contributions of the surface and bulk currents to the total dark current of the detectors with double layer passivation. The dashed lines indicate the bulk, and solid lines indicate the surface components.

In order to investigate the effect of different passivation layers, the contribution of the surface and bulk currents are shown in the same graph for 33x33 μm^2 diodes with different passivation layers (Figure 4.14). For both detectors, the dark current is totally dominated by the surface current mechanism, but surface contribution is lower for the double layer passivated detectors similar to the results obtained on the other detector structure with a cut-off wavelength of 4.1 μm.

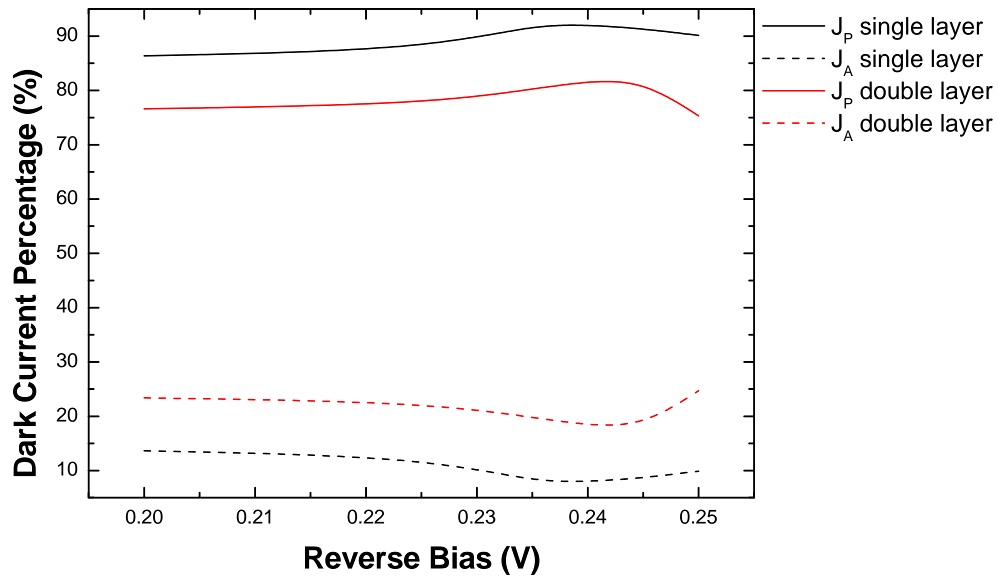

Figure 4.14: Contributions of the surface and bulk currents to the total dark current for detector size of 33x33 μm^2. The black and red lines indicate single and double layers, respectively. The dashed lines indicate the bulk, and the solid lines indicate the surface components.

The fitting results of both structures reveal that the dark current is mainly dominated by the surface current mechanisms especially in small sized detectors. A reduction of the surface current for double layer passivated photodetectors is observed after sulphur treatment in agreement with the observations of Gong *et al.* [21], Wu *et al.* [26], and Zhang *et al.* [27] for InAsSb based diodes. However, surface current is still high for both passivation layers. The optimization of sulphur treatment is required in order to achieve improved electrical characteristics.

In this chapter, dark current modeling was performed and I-V characteristics of variable area detectors were analyzed in order to isolate the surface and bulk contributions to the dark current of the diodes and to investigate the effect of different passivation layers.

CHAPTER V

CONCLUSIONS

This thesis reports a detailed characterization of $InAs_{1-x}Sb_x$ homojunction photodiodes grown on GaAs substrate by molecular beam epitaxy. In this study, a combination of a polyimide and sulphur, and a single layer polyimide were used as passivation films. Test detectors with different perimeter/area ratios were fabricated. Detailed electrical and optical characterization and noise measurements were performed for 33x33 μm^2 photodiodes. In order to identify the dominant dark current mechanisms, dark current modeling was made for 33x33 μm^2 diodes at 77 K. The dark current of the variable area test detectors was analyzed to isolate the surface and bulk current contributions.

Two different structures were used for the test detector fabrication. The optical measurements reveal that Sb mole fraction is ~0.13 and the cut-off wavelength is around 4.1 μm for the first structure. The Sb mole fraction of the second structure is 0.2 which corresponds to a cut-off wavelength of 4.8 μm at 77 K. For the first structure, the diodes yield peak detectivity of ~3.65×10^{10} $cmHz^{1/2}/W$ at 80 K. The measured zero-bias differential resistance of this diode is 0.011 Ω-cm^2 at 77 K. The peak detectivity of $InAs_{0.8}Sb_{0.2}$ detector is ~1.22×10^{10} $cmHz^{1/2}/W$ at 80 K, and the zero-bias differential resistance of this detector is 0.53 Ω-cm^2 at 77 K. The spectral

responsivity of both detectors decreased rapidly with decreasing wavelength. This can be attributed to the high recombination centers close to the substrate where most of the higher energy photons are absorbed. Dark current modeling shows that the dark currents are mainly dominated by the shunt and trap-assisted tunneling throughout the entire reverse bias. At 80 K, 1/*f* noise of the detectors seems to be dominated by TAT mechanism for both structures.

The following additional observations were made for both detector structures:

i) The dark current of the detectors with dimensions comparable to those typically used in focal plane array fabrication is dominated by surface leakage.

ii) The surface contributions are lower for the double layer (sulphur and polyimide) passivated detectors fabricated on both structures when compared with single layer (polyimide) passivated detectors.

As further work, sulphur passivation may be optimized to achieve dynamic resistance limited by bulk mechanisms in small detectors and to improve the performance of the focal plane arrays fabricated with these materials. Optimization of the detector epilayer structure and growth conditions is necessary to increase the dynamic resistance further by decreasing the bulk related components of the dark current.

REFERENCES

[1] A. Rogalski and K. Chrzanowski, "Infrared devices and techniques," *Opto-electronics Review*, vol. 10, pp. 111–136, 2002.

[2] J. D. Vincent, *Fundamentals of Infrared Detector Operation and Testing*, Wiley Press, 1990.

[3] S. Özer, "InSb and InAsSb infrared photodiodes on alternative substrates and InP/InGaAs quantum well infrared photodetectors: pixel and focal plane array performance", *Ph.D. Thesis*, Middle East Technical University, Department of Electrical and Electronics Engineering, May 2005.

[4] S. O. Kasap, *Optoelectronics and Photonics Principles and Practices,* Prentice Hall Press, 2001.

[5] A. Rogalski, *Infrared Photon Detectors*, SPIE Press, 1995.

[6] M. Henini and M. Razeghi, *Handbook of Infrared Detection Technologies,* Elsevier Science Ltd., 2002.

[7] T. P. Sun, S. C. Lee and S. J. Yang, "The current leakage mechanisms in InSb p^+n diodes," *Journal of Applied Physics Letter,* vol. 67, pp. 7092-7097, 1989.

[8] V. K. Dixit, B. V. Rodrigues, H. L. Bhat,R. Venkataraghavan, K. S. Chandrasekaran, and B. M. Arora, "Growth of InSb epitaxial layers on GaAs (001)substrates by LPE and their characterizations," *Journal of Crystal Growth,* vol. 235, pp. 154-160, 2002.

[9] G. S. Lee, P. E. Thompson, J. L. Davis and J. P. Omaggio, W. A. Schmidt, "Characterization of molecular beam epitaxially grown InSb layers and diode structures," *Solid-State Electronics,* vol. 36, pp. 387-389, 1993.

[10] I. Kimukin, N. Biyikli, E. Ozbay, "InSb high-speed photodetectors grown on GaAs substrates," *Journal of Applied Physics,* vol. 94, pp. 5414-5416, 2003.

[11] A. Tevke, C. Besikci, C. V. Hoof, and G. Borghs, "InSb infrared p-i-n photodetectors grown on GaAs coated Si substrates by molecular beam epitaxy," *Solid State Electronics,* vol. 42, pp. 1039-1044, 1998.

[12] S. Ozer and C. Besikci, "Assessment of InSb photodetectors on Si substrates," *Journal of Physics D: Applied Physics*, vol. 36, pp. 559-563, 2003.

[13] E. Michel, J. Xu, J. D. Kim, I. Ferguson, M. Razeghi, "InSb infrared photodetectors on Si ubstrates grown by molecular beam epitaxy," *IEEE Photonics Technology Letters,* vol. 8, pp. 673-675, 1996.

[14] W. Dobbelaere, J. De Boeck, P. Herremans, R. Mertens, G. Borghs, W. Luyten, and J. Van Landuyt, "$InAs_{0.85}Sb_{0.15}$ infrared photodiodes grown on GaAs and GaAs coated Si by molecular beam epitaxy," *Applied Physics Letter,* vol. 60, pp. 3256-3258, 1992.

[15] P. K. Chiang and S. M. Bedair, "p-n junction formation in InSb and $InAs_{1-x}Sb_x$ by metalorganicchemical vapor deposition", *Applied Physics Letters,* vol.46, pp. 383-385, 1985.

[16] J. D. Kim, S. Kim, D. Wu, J. Wojkowski, J. Xu, J. Piotrowski, E. Bigan, and M. Razeghi, "8-13 μm InAsSb heterojunction photodiode operating at near room temperature," *Applied Physics Letter,* vol. 67, pp. 2645-2647, 1995.

[17] P. Chakrabarti, A. Krier, X. L. Huang, and P. Fenge, "Fabrication and characterization of an $InAs_{0.96}Sb_{0.04}$ photodetector for MIR applications," *IEEE Electron Device Letters,* vol. 25, pp. 283-285, 2004.

[18] C. Besikci, S. Ozer, C.V. Hoof, L. Zimmermann, J. John and P. Merken, "Characteristics of $InAs_{0.8}Sb_{0.2}$ photodetectors on GaAs substrates," *Semiconductor Science and Technology,* vol. 16, pp. 992-996, 2001.

[19] K. Mohammed, F. Capasso, R. A. Logan, J. P. van der Ziel, and A. L. Hutchinson, "High-detectivity $InAs_{0.85}Sb_{0.15}$/InAs infrared (1.8-4.8 μm) detectors," *Electronic Letters*, vol. 22, pp. 215-216, 1986.

[20] P. Norton, "HgCdTe infrared detectors," *Opto-Electronics Review,* vol. 10, pp. 159-174, 2002.

[21] X. Y. Gong, T. Yamaguchi, T. Makino, K. Ohshimo, M. Aoyama, M. Kumagawa, N. L. Rowell, R. Rinfret, "Sulphur passivation of InAs(Sb)," *Applied Surface Science,* vol. 113, pp. 388-392, 1996.

[22] T. P. Sun and S. C. Lee, "The current leakage mechanism in InSb p^+n diodes," *Journal of Applied Physics,* vol. 67, pp. 7092-7097, 1990.

[23] I. Bloom and Y. Nemirovsky, "Surface passivation of backside-illumibated indium antimonide focal plane array," *IEEE Transactions on Electron Devices,* vol. 40, pp. 309-314, 1993.

[24] Z. Clahorra, J. Bregman and Y. Shapira, "Studies of SiO_x anodic native oxide interfaces on InSb," *Journal of Vacuum Science and Technology,* vol. 4, pp. 1195-1202, 1986.

[25] J. Breggman, Y. Shapira and Z. Calahorra, "Correlations between the chemical and electronic structure of thermally treated anodized InSb," *Journal of Vacuum Science and Technology,* vol. 4, pp. 1432-1436, 1986.

[26] B.H. Wu, G.Q. Xia, Z.H. Li, J. Zhou, "Sulphur passivation of the InGaAsSb/GaSb photodiodes," *Applied Physics Letter,* vol. 80, pp. 1300-1305, 2002.

[27] X. Zhang, A.Z. Li, C. Lin, Y.L. Zheng, G.Y. Xu, M. Qi, Y.G. Zhang, "The effects of $(NH_4)_2S$ passivation treatment on the dark current –voltage characteristics of InGaAsSb PIN detectors," *Journal of Crystal Growth,* vol. 251, pp. 782-786, 2003.

[28] U. Tumkaya, "Performance assessment of indium antimonide photodetectors on silicon substrates", *M.Sc.Thesis,* Middle East Technical University, Departmant of Physics, June 2003.

[29] Y. Nemirovsky and A. Unikovsky, "Tunneling and 1/*f* noise currents in HgCdTe photodiodes," *J. Vac. Sci. Technol. B*, vol. 10, pp. 1602-1610, 1992.

[30] V. Gopal, S. K. Singh, R. M. Mehra, "Analysis of dark current contributions in mercury cadmium telluride junction diodes," *Infrared Physics & Technology*, vol. 43, pp. 317-326, 2002.

[31] Y. Nemirovsky, R. Fastow, M. Meyassed, and A. Unikovsky, "Trapping effects in HgCdTe," *J. Vac. Sci. Technol. B*, vol. 9, pp. 1829-1839, 1991.

[32] A. Rogalski, *Narrow-Gap Semiconductor Photodiodes*, SPIE Press, 2000.

[33] R. K. Lal, M. Jain, S. Gupta, P. Chakrabarti, "An analytical model of a double heterostructure mid-infrared photodetector," *Infrared Physics & Technology,* vol. 44, pp. 125-132, 2003.

[34] S. M. Johnson, D. R. Rhiger, J. P. Rosbeck, J. M. Peterson, S. M. Taylor, and M. E. Boyd, "Effect of dislocations on the electrical and optical properties of long-wavelength infrared HgCdTe photovoltaic detectors," *J. Vac. Sci. Technol. B*, vol. 10, pp. 1499-1506, 1992.